Revision 2

The ore-forming magmatic-hydrothermal system of the Piaotang W-Sn deposit (Jiangxi, China) as seen from Li-mica geochemistry

Hélène Legros [a,b,*], Christian Marignac [a,c], Thomas Tabary [d,a], Julien Mercadier [a], Antonin Richard [a], Michel Cuney [a], Ru-Cheng Wang [e], Nicolas Charles [b], Marc-Yves Lespinasse [a]

[a] *Université de Lorraine, CNRS, CREGU, GeoRessources, Boulevard des Aiguillettes B.P. 70239, F-54506 Vandoeuvre-lès-Nancy, France*

[b] *BRGM-French Geological Survey, 3, Av. Claude Guillemin, BP 36009, 45060 Orléans Cedex 2, France*

[c] *Ecole Nationale Supérieure des Mines de Nancy, Parc de Saurupt, F-54042 Nancy, France*

[d] *Institut Polytechnique LaSalle Beauvais - 19 rue Pierre Waguet- BP30313 - F-60026 BEAUVAIS Cedex, France*

[e] *State Key Laboratory for Mineral Deposits Research, School of Earth Sciences and Engineering, Nanjing University, Xianlin University Town, Nanjing 210046- China*

* GeoRessources UMR 7359, Université de Lorraine, Faculté des Sciences et Technologies, Entrée 3B - bureau A609, Boulevard des Aiguillettes BP 70239, 54506 Vandoeuvre-lès-Nancy Cedex, France

Phone : +33 3 83 68 47 69

Mail : helene.legros@univ-lorraine.fr

This is a preprint, the final version is subject to change, of the American Mineralogist (MSA)
Cite as Authors (Year) Title. American Mineralogist, in press.
DOI: http://dx.doi.org/10.2138/am-2018-6196

Abstract

Many studies have proved the usefulness of Li-mica and chlorite geochemistry as indicators of the chemical and thermal evolution of magmatic systems. This study highlights the suitability of Li-micas as tracers of hydrothermal mineralizing events in world-class W-Sn deposits associated with Jurassic (190–150 Ma) granites in China through the complex magmatic–hydrothermal evolution of the Piaotang deposit (South Jiangxi). A paragenetic sequence has been established for the Piaotang deposit comprising (i) a first "silicate-oxide" stage that hosts abundant W-Sn mineralization (wolframite and cassiterite), (ii) a "calcic" stage with scheelite and wolframite, (iii) a "base metal sulphides" stage with cassiterite and wolframite, and (iv) a late "sulphide" stage, involving for the first time a polyphase emplacement of the mineralization. Li-micas from the underlying granite, greisen, and the different stages represented in the veins, were studied. The chemistry of the micas (characterized by intermediate compositions between phlogopite-zinnwaldite-muscovite poles) demonstrates the presence of end-members representing three different fluids that were involved in the emplacement of the Piaotang deposit. These end-members can be linked to previous fluid inclusion studies conducted on this deposit. The three fluids are identified to be magmatic, meteoric (as previously reported in the literature), and also metamorphic, and are shown to have mixed throughout the different stages. Moreover, it appears that the magmatic fluids could not have been derived from the Piaotang biotite granite but rather must have originated from a more evolved rare metal granite that is presently unidentified. These fluids were responsible for the greisenization.

Finally, chlorite geochemistry reveals the occurrence of a heating process (from 200°C in stage II to 300°C in stage III) during the post-mineralizing stages, which was responsible for the precipitation of new generations of ore-bearing minerals (cassiterite and wolframite)

concomitant with a continuous gain of metals during the emplacement of the Piaotang deposit.

Keywords

Piaotang, W-Sn deposit, Yanshanian, Lithium-mica, Chlorite, Magmatic-hydrothermal

Introduction

Constraining the origin and evolution of mineralizing fluids in W-Sn-quartz vein-type deposits remains challenging. Current models refer to (i) metal-rich magmatic fluids exsolved from granitic magmas (e.g., Kamenetsky et al., 2004; Audétat et al., 1998; Thomas et al., 2005), (ii) "external" fluids (metamorphic or meteoric) that circulate around cooling peraluminous granitoids and leach metals from the peraluminous granitoid or the country rocks (e.g., Wilkinson 1990; Blamart 1991; Smith et al. 1996; Zhao and Jiang, 2004), or (iii) combinations of the two (e.g., Beuchat et al., 2004; Carruzzo et al., 2004; Marignac and Cathelineau 2009; Wei et al., 2012; Chicharro et al., 2016). In association with stable isotope (O, H) studies of minerals (Beuchat et al., 2004; Carruzzo et al., 2004; Wei et al., 2012; Chicharro et al., 2016), fluid inclusion studies have contributed greatly to these models in recent years, by providing valuable information about the origins and physical–chemical evolution of the mineralizing fluids (e.g., Audétat et al. 1998; Beuchat et al., 2004; Carruzzo et al., 2004; Wei et al., 2012; Chicharro et al., 2016). However, fluid inclusion studies are restricted to just a few favourable mineral species (e.g., topaz, quartz, wolframite, and cassiterite) and even then, primary fluid inclusions are often hard to identify. Consequently, several stages of the deposit formation cannot be studied by this approach, and can only be

investigated indirectly using detailed paragenetic successions and in-depth geochemical analysis. In this perspective, Li-mica and chlorites, which are frequently found in W–Sn vein-type deposits (Giuliani, 1985; Tischendorff et al., 1997; Costi et al., 2002; Johan et al., 2012; Nieva, 2013) show interesting potential. The majority of chlorite species are sensitive to temperature in hydrothermal and geothermal systems (Walshe, 1986), and thus provide a useful geothermometer in many geological settings and, in particular, in hydrothermal metallogenic systems. Moreover, Legros et al. (2016) showed that, in the case of the Maoping deposit (Jiangxi, China), the detailed chemistry of magmatic and hydrothermal Li-mica can be used to interpret the relative contributions of magmatic, meteoric and metamorphic fluids in the formation and evolution of W-Sn deposits. Based on this work, the present study focuses on the Piaotang W-Sn deposit, located in the southern Jiangxi Metallogenic Province (SE China), the most important W-Sn province in the world (USGS, 2016). The Piaotang W–Sn deposit exhibits several generations of magmatic and hydrothermal Li-mica, as well as two generations of chlorite, that crystallized during multiple stages of the ore-forming system. This study uses combined optical microscopy, SEM, EPMA and LA-ICPMS to establish for the first time a detailed paragenetic succession for the Piaotang deposit and to determine the major and trace element compositions of Li-mica and chlorite geothermometers, with the aim of providing new constraints on the physical–chemical evolution of fluids involved in the formation of such deposits.

Geological Setting and sampling

The southern Jiangxi Metallogenic Province

The southern Jiangxi W-Sn province, also referred as Nanling metallogenic belt, is located in the Cathaysia Block of the South China Craton (SCC) and is currently the main W repository in China (90% of the reserves: Wang et al. 2016). The SCC resulted from late Grenvillian suturing between two terranes: the Yangtze Block to the north and the Cathaysia Block to the south, during the Jiangnan orogeny (Charvet 2013 and references therein). The final age of the collision is still under debate, with estimates ranging between 900 and 800 Ma (e.g., Li et al. 2009, Hu and Zhou 2012, Yao et al. 2013). Mostly coinciding with the southern boundary of the orogen, the major Jiangshan-Shaoxi fault zone is considered the northern boundary of the Cathaysia block (Figure 1).

After the Neoproterozoic collage of the Yangtze and Cathaysia terranes, the newly formed SCC was strongly reworked, becoming progressively metacratonized through a sequence of intra-continental events starting in the late Neoproterozoic (the failed Nanhua Rift: Wang et al. 2006), and followed by the Middle Palaeozoic ("Caledonian") Kwangsian orogenesis, the Early Mesozoic Indosinian events and the Jurassic-Cretaceous Yanshanian events. Although the entire SCC was affected, the metacratonisation and the most pervasive magmatic activity during the Yanshanian were observed in the Cathaysia Block. Consequently, the Phanerozoic magmatism was responsible for producing one of the largest igneous provinces in the world (Zhang et al. 2012, Wang et al. 2013). A variety of granites were produced, including S-, I- and peralkaline-types. Metaluminous A-type granites remain the most frequently found. Nb-Ta-rich peraluminous rare metal granites (RMG) also form part of this magmatic diversity. Sporadic occurrences of RMG were first recorded in the Kwangsian (Wang et al., 2011), whereas both the Indosinian (270–200 Ma) (with the world-class Yichun deposit) and the early Cretaceous (ca. 130 Ma) appear to have been the most productive episodes of RMG magmatism.

The Middle Palaeozoic Kwangsian (Caledonian) orogeny, which produced a double-verging NE-trending belt, is commonly interpreted to have resulted from the inversion of the Nanhua Rift (e.g., Charvet et al., 2010, Charvet 2013). This first intra-cratonic event, which was restricted to the Cathaysia Block, culminated with crustal thickening and a HT metamorphic event at ca. 450 Ma, yielding a high-grade belt composed of migmatites and granulites (e.g., Liu et al. 2010), followed by basaltic underplating, dehydration melting in the lower crust, and the emplacement of large syn-kinematic S-type granite bodies (covering more than 20,000 km²: Li et al. 2011) at ca. 430–420 Ma (e.g., Wang et al. 2013, Xia et al. 2014).

At the end of the Triassic, a second major intracratonic event, which reworked the earlier Kwangsian structures (with the same NE-trending direction but a NW vergence), recorded the suturing of the SCC with the North China craton (e.g., Wang et al. 2001). This Indosinian event, which affected both the Cathaysia Block and the Jiangnan orogen, was associated with HT metamorphism (metamorphic core complexes: Faure et al. 1996), and produced large volumes of magma (presently covering 14,300 km^2), with the subsequent emplacement of I-type granites (245-230 Ma) and S-type granites (220-210 Ma) (Shu et al. 2008 and references therein). The first cycle of Nb–Ta granites occurred in the Nanling Range (Mao et al. 2013).

The Yanshanian event (Late Jurassic-Cretaceous) was essentially marked by magmatism that led to the generation of the large igneous province (Li et al., 2014). However, the event was also associated with alternating transpressive and transtensional deformation along the same NE-SW lineaments that controlled the Kwangsian and Indosinian events (Li et al., 2014, Liu et al., 2012, Shu et al., 2009). The Yanshanian events are currently interpreted as reflecting a major change in the overall plate tectonic regime, with a shift from a Palaeo-Tethysian to a Pacific control, marked by the inception of subduction of the Paleo-Pacific (Izanagi) plate under the SCC (e.g. Zhou et al., 2002). The Yanshanian is subdivided into the Early (Jurassic)

and Late (Cretaceous) Yanshanian. The Jurassic (190–150 Ma) is characterized by extensive magmatic activity, today represented by the outcropping of granitic rocks over an area of about 100,000 km^2. The peak of magmatic activity is dated at 160–150 Ma, with several pulses, and the granitic province exhibits all the characteristics of a felsic large igneous province. The majority of the Cathaysia W-Sn deposits were formed during the same 160–150 Ma interval, although this was recently challenged (ca. 130 Ma ages proposed by Wang et al. 2016). Coeval with this, the E-W trending Nanling Range, which is composed of three roughly parallel granitic belts and associated wolframite deposits (Zhao et al. 2017), was formed. The Cretaceous event (135–80 Ma) was characterized by granites (mainly intruded in the Cathaysian interior) and rhyolites (mainly erupted along the coastal area). Renewed rare-metal deposition occurred in the Nanling Range, characterized notably by large magmatic-related Sn and U mineralizations, while Au-Cu-Pb-Zn-Ag mineralizations were deposited along the southeastern coast (Hua et al., 2005).

The Piaotang W-Sn deposit

The polymetallic W-Sn-(Nb) Piaotang deposit is one of several giant tungsten deposits in the Nanling Range and produces 1,500 t WO_3 per year, ranking it eighth in the top ten reserves in China with 47,775 t WO_3 (MB Company database: www.metalbulletin.com). The deposit is composed of mineralised veins emplaced in Cambrian metasediments that lie above the concealed Piaotang biotite granite (Figure 2). Two sets of faults can be observed in the field: E-W-oriented faults intersecting NE-SW-oriented faults (Figure 2A). The granite was emplaced during the Jurassic (159.8 ± 0.3 Ma, U-Pb zircon dating; Zhang et al., 2017), coeval with the W mineralization (159.5±1.5 Ma, U-Pb cassiterite dating; Zhang et al., 2017). A

Kwangsian quartz diorite body (439 ± 2 Ma, U-Pb zircon dating; He et al. 2010) also occurs at depth.

The vein system: The vein system extends vertically over 300 m, down to the Piaotang biotite granite (Figure 2B). The vein system includes flat-lying and steep veins, associated with evidence for brittle tectonics. Field observations at different levels show (i) a first generation of, more or less lenticular, flat-lying (N80-90°E 30-40°N) quartz veins, displaying some evidence of faint extensional tectonics, (ii) a second generation of similar flat-lying veins (N0-30°E 30-40°W) corresponding to inverse faulting (as demonstrated by their intersections with the first generation veins), and (iii) a third generation of steep veins, with clear evidence for both faint inverse and sinistral strike-slip tectonics. Whereas the first generation of veins is scarce and the second generation is moderately frequent, the third generation of veins is ubiquitous. Only the third generation of veins shows mineralizations of economic interest. The thickness of the veins increases from the bottom to the top, from a few centimetres at the 556 level, to more than one meter at the 268 level.

Relationship with the granite: At the bottom of the system, a fine-grained biotite granite is observed. The interaction between this granite and the vein system appears to be complex.

- The granite exhibits a locally steep and sharp contact with the country rocks, striking 30°N. Outside the main body, several gently dipping dike-like expansions are observed, which themselves present complex digitations in the form of crackle breccias. No ductile deformation is observed along the contact between the granite and country rocks.

- Inside the granite body, a gently dipping vein system is observed. The veins show borders composed of feather-like K-feldspars megacrysts, and a filling of greisenized fine-grained rock that forms a cement around large quartz crystals (stockscheider).

- The granite overprints a generation of flat-lying quartz veins which likely represent the first generation of veins. Some dike-like expansions appear to be associated with inverse brittle faulting as they intersect earlier flat-lying quartz veins. These dikes are likely coeval with the second generation of veins.

Granite and greisen: The primary granite mineralogy consists of quartz, orthoclase, albite and biotite (see below, Figure 5a). The texture is microgranular with porphyric perthitic K-feldspar and quartz. No ductile or brittle deformation is observed: the granite is always macroscopically isotropic. The micas enclose a variety of accessory minerals—apatite, quartz, xenotime, rutile, monazite, fluorite and zircon—that are not observed in quartz or feldspars. W, Sn or Nb-Ta minerals have not been observed in the granite. The feldspars are altered to muscovite but also exhibit clay mineral alteration. This may be considered as incipient greisenization, even if a clear granite to greisen transition is not observed in the mine.

The greisen at the top of the granite body is composed exclusively of quartz, muscovite and fluorite (see below, Figure 5b). All minerals are corroded and very weakly deformed. Fluorite is observed exclusively as inclusions in muscovite.

Analytical methods

Thirty samples of the mineralized veins, granite and greisen (Figure 3) were collected in the Piaotang mine site at the 268, 388 and 556 levels (respective depths). The relationships between host-rocks and veins are easily observed in the mine. As discussed previously, the third generation of veins is the mineralization-bearing vein and thus only this vein is considered in the remainder of the manuscript.

All preparations and analyses described below were carried out at the GeoRessources laboratory (Nancy, France). Petrographic observations were performed on polished thin-sections using conventional transmitted and reflected light microscopy and a HITACHI FEG S4800 scanning electron microscope (SEM) equipped with an energy dispersive spectrometer (EDS), using a Si(Li) semi-conductor detector.

Electron microprobe analyses (EMPA) of Si, Al, Ti, Na, Mg, Mn, Fe, K, Ca, Rb and F were performed on chlorites and Li-bearing micas using a CAMECA SX100 instrument equipped with a wavelength dispersive spectrometer (WDS) and calibrated using natural and synthetic oxides and silicates (albite, olivine, Al_2O_3, orthose, andradite, $MnTiO_3$, hematite, cassiterite, $RbTiPO_5$, topaz, scheelite, $LiTaO_3$ and $LiNbO_3$). A current of 12nA and an accelerating voltage of 15kV was used with a counting time of 10s per element. Special attention was paid to fluorine determination by using a spectrometer dedicated to this element (average detection limit of 1300 ppm). The analyses have a spatial resolution of 1 to 2 µm. The reproducibility of standard analyses was 1% for each element analyzed. Total Fe is presented as FeO.

Major, minor and trace elements (^{24}Mg, ^{27}Al, ^{28}Si, ^{47}Ti, ^{55}Mn, ^{59}Co, ^{93}Nb, ^{95}Mo, ^{118}Sn, ^{137}Ba, ^{181}Ta, ^{182}W) were measured in Li-bearing micas using a LA-ICPMS instrumental setup described in Leisen et al. (2012) and Lach et al. (2013), composed of a GeoLas excimer laser (ArF, 193 nm, Microlas, Göttingen, Germany) (Günther et al., 1997) and an Agilent 7500c quadrupole ICPMS. The laser beam was focused onto the sample within a 24.5 cm^3 cylindrical ablation cell with a Schwarzschild reflective objective (magnification ×25; numerical aperture 0.4) mounted on an optical microscope (Olympus BX41), equipped with a X–Y motorized stage and a CCD camera. Si (determined by EPMA) was chosen as an internal standard and precisely quantified by EPMA for all analysed micas. NIST SRM 610 (values from Jochum et al., 2011) was chosen as the external standard (accuracy was verified by analysing NIST SRM 612). The parameters used were a fluence of 8J/cm² and a laser shot

243 frequency of 5 Hz, He = 0.5 L.min^{-1} as a carrier gas mixed with Ar = 0.7 L.min^{-1} via a
244 cyclone mixer prior to entering the ICP torch, spot sizes of 120 μm, and an ablation duration
245 of 40 s. Quantifications were performed using Iolite software (Paton et al., 2011) and
246 concentrations were calculated following Longerich et al. (1996).
247 The temperature of chlorite formation was calculated using the graphical geothermometer of
248 Cathelineau and Bourdelle (2015) for each composition that plotted between the sudoite,
249 corundophilite and Al-free chlorite end-members on the Si-R^{2+} diagram of Wiewiora and
250 Weiss (1990). This method assumes that quartz and water activities are equal to 1 and is valid
251 for a temperature range of 50–350°C, which seems reasonable in the case of quartz-bearing
252 rocks formed under low-grade metamorphic conditions, such as those in the Piaotang deposit.
253 All Fe was assumed to be ferrous in the calculations of the structural formulas.
254
255 **Paragenetic sequence**
256
257 A paragenetic succession was previously established by Tanelli (1982), providing a common
258 chart for the Piaotang and Xihuashan deposits. According to Tanelli (1982), the succession
259 can be divided into three stages: (i) a first "oxide stage" with quartz, K-feldspar, beryl, topaz,
260 wolframite and cassiterite; (ii) a second "sulphide stage" with quartz, bismuthinite, sphalerite,
261 galena, cassiterite and wolframite; and (iii) a third "carbonate stage" with quartz, chlorite,
262 sericite, fluorite, calcite, pyrite and scheelite.
263 In the present study, a new paragenetic sequence was established from field observations in
264 the mine galleries, as well as from petrographic observations by optical microscope, SEM and
265 EPMA analyses in the laboratory (Figure 4). Hereafter, minerals refer to (i) their
266 recommended IMA mineral abbreviations, (ii) their generation number (1 to 4, from the oldest
267 to the youngest), and (iii) the paragenetic stage to which they belong (I to III, from the oldest

to the youngest). For example, $Wf_{2\text{-III}}$ stands for the second generation of wolframite in the whole paragenetic sequence, occurring during stage III (sulphide stage).

As seen in Figure 4, our detailed study has led to some modification of the Piaotang paragenetic succession. The main difference is seen in the "calcic stage", now intercalated between the "oxide" and "sulphide" stage on the basis of crosscutting relationships between major minerals of the different stages. The succession obtained in this study is valid for the entire vertical extent of the mineralized system (all levels).

The silicate-oxide stage (Stage I) represents the main stage of crystallization of the ore-bearing minerals, wolframite and cassiterite. The Stage I minerals are Fe-Li-mica (Fe-Li-$mca_{1,2,3\text{-I}}$), cassiterite ($Cst_{1,2\text{-I}}$), wolframite ($Wf_{1\text{-I}}$), topaz ($Toz_{1\text{-I}}$), quartz ($Qtz_{1,2\text{-I}}$), molybdenite ($Mlb_{1\text{-I}}$), and possibly beryl ($Brl_{1\text{-I}}$). Stage I can be subdivided into two sub-stages: the first (Ia) is the main ore stage and the second (Ib) is the main Fe-Li mica stage. There is however, considerable overlap: (i) the earliest Fe-Li-$mca_{1\text{-I}}$ are coeval with $Cst_{1\text{-I}}$, and (ii) $Cst_{2\text{-I}}$ is observed to have crystallized coevally with later Fe-Li-$mca_{2\text{-I}}$.

The wolframite $Wf_{1\text{-I}}$ shows maximum growth perpendicular to the walls, with crystals up to 15 cm in size found in the largest veins (Figure 3). $Wf_{1\text{-I}}$ is coeval with quartz growth ($Qtz_{1\text{-I}}$), which shares similar comb textures and size. However, the initial morphologies of both the quartz and wolframite were considerably altered by a succession of crack-seals (up to brecciation) and recrystallization phenomena, with the growth of small newly formed wolframite prisms on previous crystals (Figure 5c). Nevertheless, the wolframite composition is homogeneous, with an average structural formula of $Fe_{0.5}Mn_{0.5}WO_4$ (SEM). The main cassiterite ($Cst_{1\text{-I}}$) crystallization occurred after the main wolframite deposition, and cassiterite growth is often observed on wolframite crystals (Figure 5c). $Cst_{1\text{-I}}$ deposition was coeval with crack-sealing and $Cst_{1\text{-I}}$ is therefore frequently found at the vein selvages. The cassiterite

292 composition is pure SnO_2 (SEM). The earliest Fe-Li-mca$_{1\text{-}I}$ are associated with Cst$_{1\text{-}I}$, and
293 have often grown in dissolution cavities affecting Qtz$_{1\text{-}I}$ (Figure 5d). A second generation of
294 Fe-Li mica (Fe-Li-mca$_{2\text{-}I}$) occurs as infilling of vein openings, most often at the vein selvage,
295 where it separates early cassiterite from the wall-rocks. Small overgrowths of Cst$_{2\text{-}I}$ are
296 observed at the mica-Cst$_{1\text{-}I}$ boundary. Crack-seals filled with Fe-Li-mca$_{2\text{-}I}$ are also observed
297 within Fe-Li-mca$_{1\text{-}I}$ aggregates and Cst$_{1\text{-}I}$, with overgrowths of Cst$_{2\text{-}I}$ associated with Qtz$_{2\text{-}I}$.
298 Cst$_{2\text{-}I}$ is compositionally identical to Cst$_{1\text{-}I}$. A last episode of crack-seal is observed in Fe-Li-
299 mca$_{2\text{-}I}$ at the vein boundary and is associated with the deposition of the third generation of Fe-
300 Li micas (Fe-Li-mca$_{3\text{-}I}$).

301 Topaz (Toz$_{1\text{-}I}$) has been deposited in fractures affecting Qtz$_{1\text{-}I}$, with symplectic topaz-quartz
302 local associations indicating partial dissolution of the quartz. The exact timing of the topaz
303 deposition is ambiguous. Local observations indicate that the topaz post-dates the Cst$_{1\text{-}I}$
304 deposition and has been altered by stage III micas, but no relationship between the topaz and
305 the main micas was observed. Topaz was most probably emplaced during stage I as it
306 experienced the same plastic deformation as the surrounding Qtz$_{1\text{-}I}$ as well as molybdenite
307 (see below).

308 Tanelli (1982) listed K-feldspar, beryl, tourmaline, helvite and biotite in the oxide stage.
309 These minerals were not observed in the present study, with the possible exception of beryl.
310 Some euhedral prismatic crystals with hexagonal sections are observed in association with
311 Qtz$_{1\text{-}I}$, which, being totally pseudomorphosed by stage III Li-msc$_{4\text{-}III}$, could originally have
312 been beryl (Brl$_{1\text{-}I}$).

313 An episode of ductile deformation separates stage I from stage II. This episode affected both
314 Qtz$_{1,2\text{-}I}$, all the Fe-Li micas, the topaz and the molybdenite. This deformation consists of very
315 low intensity kinking of the micas and molybdenite, but is pervasive in quartz (subgrain

316 boundaries, undulose extinction). Such ductile-brittle transition separation (only observed
317 microscopically) between early minerals and later stage minerals was also observed in the
318 nearby Maoping deposit (Legros et al. 2016), where it may have been related to extensional
319 tectonics.

320 *Calcic stage II*: Stage II is characterized by the partial transformation of wolframite into
321 scheelite ($Sch_{1\text{-}II}$), followed by a first generation of chlorite ($Chl_{1\text{-}II}$) and fluorite ($Fl_{1\text{-}II}$)
322 (Figure 6a and b). Small euhedral prismatic crystals of W-rich (up to 8.5 wt% WO_3)
323 mangano-columbite ($Clb_{1\text{-}II}$), up to 5 μm in size, are systematically dispersed in the $Chl_{1\text{-}II}$. It
324 is likely that the $Clb_{1\text{-}II}$ is the result of mobilization of Nb and W during wolframite
325 transformation into scheelite. However, no particular textures were observed in $Wf_{1\text{-}I}$ using
326 the SEM.

327 *Sulphide stage III*: Although mainly marked at the macroscopic scale by sulphide deposition,
328 this stage is characterized by a complex succession of phyllosilicates, sulphides and late
329 wolframite and cassiterite. The Fe-Li-mica (Fe-Li-$mca_{4\text{-}III}$) developed first, mainly at the
330 expense of a pervasively corroded $Qtz_{1,2\text{-}I}$ or in the form of small veinlets overprinting earlier
331 minerals as $Chl_{1\text{-}II}$. Fe-Li-$mca_{4\text{-}III}$ is also observed in thin crack-seal re-openings at the vein
332 boundaries (exhibiting shearing features) and in alteration of $Toz_{1\text{-}I}$ (Figure 6c). Fe-Li-$mca_{4\text{-}III}$
333 also appears as spherolites (up to 150 μm in diameter) in vuggy microcavities. Some
334 overgrowths on earlier micas (mainly Fe-Li-$mca_{1\text{-}I}$) are associated with these spherolites. As
335 seen in Figure 7, these overgrowths (Z1 to Z4) are zoned and associated with reworking of the
336 early zinnwaldite/Li-Ms association, which is overprinted by micas similar to the first zone of
337 the overgrowth. The zones consist of an alternation of Li-Fe-Ms and Li-Ms. In the Monier
338 and Robert diagram (1986) (Figure 8c), these zones plot along the Fe-Li-$mca_{4\text{-}III}$ trend. The
339 end of the overgrowth is marked by distinctly Mg-rich (and Mn-poor) compositions, very

similar to those of the Fe-Li-mca$_{4\text{-III}}$ micas (Figure 7). Consequently, these overgrowths are considered to be coeval with the latter (Fe-Li-mca$_{4b\text{-III}}$). Sulphide deposition, coeval with a second generation of chlorite (Chl$_{2\text{-III}}$) (Figure 6d), follows chalcopyrite deposition (Ccp$_{1\text{-III}}$). Small euhedral prisms of a phenakite (Phk$_{1\text{-III}}$) are found as inclusions in the chalcopyrite. This phenakite could have trapped the beryllium leached from Brl$_{1\text{-I}}$ when replaced by Fe-Li-mca$_{4\text{-III}}$. Chl$_{2\text{-III}}$ deposition started with a Fe-chamosite composition and then evolved towards an Al-Fe clinochlore composition. Sphalerite (Sp$_{1\text{-III}}$) and stannite (Stn$_{1\text{-III}}$) followed the chalcopyrite deposition and appear as trails of more-or-less rounded inclusions (a few tens of μm in size). In detail, the sphalerite inclusions are zoned, with a core that is spotted with multiple chalcopyrite micro-inclusions and a rim that exhibits symplectic stannite-sphalerite associations (Figure 6e). Chalcopyrite micro-inclusions in sphalerite are known as "chalcopyrite disease", which is classically interpreted to result from a reaction between sphalerite and a permeating Cu-rich fluid (Barton et al., 1978, Bortnikov et al., 1991). In the present case, the texture could therefore be referred to as "sphalerite disease", interpreted as the healing of cracks affecting chalcopyrite. In systematic spatial association with sphalerite and stannite in the chalcopyrite, small euhedral cassiterite crystals (Cst$_{3\text{-III}}$) are observed, which locally contain inclusions of Mn-wolframite ($Fe_{0.43}Mn_{0.57}WO_4$, Wf$_{2\text{-III}}$) (Figure 6f). Cst$_{3\text{-III}}$ is also present in the form of microcracks lining the chalcopyrite boundary. Wf$_{2\text{-III}}$ microcracks of hübneritic composition (from $Fe_{0.20}Mn_{0.80}W0_4$ to $Fe_{0.12}Mn_{0.88}WO_4$) are also observed. A late fluorite (Fl$_{2\text{-III}}$) is coeval with Cst$_{3\text{-III}}$ and Wf$_{2\text{-III}}$ (Figure 5f and g).

Sulfosalt stage IV: Overprinting all preceding mineral assemblages, a late generation of sulphured minerals has precipitated in the following sequence: galena (Bi-rich, up to 1 wt%), members of the lillianite series ($Ag_{0.8\text{-}1.1}Pb_{1.6\text{-}1.3}Bi_{2.6\text{-}2.7}S_6$), lead-rich bismuthinite (up to 5 wt%), and finally, native bismuth (Figure 6h).

Composition of micas

Major elements

All mica generations from the granite, greisen and the veins were studied by SEM and analysed by EPMA for major elements and LA-ICPMS for minor and trace elements. Representative EPMA analyses are presented in Table 1. A total of 170 EPMA and 98 LA-ICPMS analyses were performed.

The problem of Li content: The LA-ICPMS analyses (Table 2) showed that all Piaotang micas are Li-bearing micas. However, the micas appear to display complex internal patterns (see below) and the diameter of the LA-ICPMS spots (44 to 120 μm) was not small enough to measure most of the microstructures related to EPMA measurements (internal standardization for LA-ICPMS). Moreover, being a highly volatile element, lithium remains difficult to quantify with precision by LA-ICPMS (up to 0.5 wt. % Li_2O). To avoid this "lithium issue", the empirical regressions of Tischendorff et al. (1997) are used. The suitable regressions in our system would be SiO_2 for tri-octahedral micas and F for di-octahedral micas, and both were used in the present study. However, the results were inconsistent: in the Li-Al-R^{2+} diagram of Foster (1960), the Piaotang micas plot within the immiscibility gap determined by Monier and Robert (1986), meaning that our calculated LiO_2 contents (Li_2O*) are underestimated. This problem was also encountered by Legros et al. (2016) in a study of the Maoping deposit and was resolved by adjusting the Li_2O* contents (by adding a constant to the Li_2O* values estimates from the Tischendorff et al. (1997) regressions). However, this method would be very complicated to apply in the case of the Piaotang deposit, where more

388 trends are exhibited (Figure 8). Consequently, the lithium content of the micas has been
389 removed from the diagrams.

390 *Micas from granite*: With an average Fe# (Fe/(Fe+Mg+Mn) ratio) of 0.55 and an average
391 $R^{2+}/(R^{2+}+Al)$ of 0.53, the granite micas plot between annite-phlogopite and eastonite-
392 siderophyllite compositions (Figure 8a) and may be classified as lithian biotite.

393 *Fe-Li-mca$_{1,2\text{-}I}$*: The two first generations of micas appear as intergrowths of tri-octahedral and
394 di-octahedral components. Two converging trends are displayed in the Monier and Robert
395 (1986) diagram (Figure 8b): (i) a zinnwaldite-phlogopite trend (referred to as zinnwaldite in
396 the following) and (ii) a trend towards Li-muscovite (about 0.5 trilithionite), referred to as Fe-
397 Li muscovite in the following (Figure 8b). In detail, the micas consist of a succession of
398 alternating compositions between Fe-Li muscovite (Li-Fe-ms) and zinnwaldite (Znw). Both
399 Li-Fe-ms and Znw show a significant manganese content even though the zinnwaldite
400 components always exhibit higher Mn contents (up to 1.9 wt. % MnO). In addition, the
401 earliest Fe-Li-mca$_{1\text{-}I}$ are characterized by the development of a large overgrowth, on a core
402 formed by the complex intergrowths described above (Figure 7). This overgrowth is zoned,
403 showing a succession of Fe-Li-ms toward Li-ms trends with distinct Fe#, similar to the
404 composition of the core (Figure 7). In addition, the outer zones are characterized by very low
405 Fe# and Mn contents.

406 *End of stage I micas*: The Fe-Li-mca$_{3\text{-}I}$ are either Znw or Li-Fe-ms, and exhibit very similar
407 compositions to the earliest Fe-Li micas (Figure 8b).

408 *Stage III micas*: The Fe-Li-mca$_{4\text{-}III}$ micas are all Fe-Li-ms, which, in the Al-Si-R^{2+} diagram,
409 are displaced from their equivalent from stage I (Figure 8c). However, they exhibit distinctive
410 low Fe# (0.2–0.4) and MnO (less than 1.0 wt. %) contents.

411 *Greisen*: The greisen micas are Fe-Li-ms, which, in the Monier and Robert (1986) diagram,
412 are very similar to the Fe-Li-mca$_{1\text{-}I}$ and Fe-Li-mca$_{3\text{-}I}$ Fe-Li muscovites.

413 It is noteworthy that these data exhibit similar trends to the Maoping Li-micas analysed by
414 Legros et al. (2016) in the same district (Figure 8d).

415

416 **Trace elements**

417

418 *Micas from granite:* These micas are characterized by elevated Nb and Ta contents
419 (Nb+Ta>100 ppm; Figure 9a), with variable Nb# (Nb/(Nb+Ta)) ranging from 0.91 to 0.67.
420 They have the lowest W (<10 ppm) and Sn (<200 ppm) contents of all micas analysed in this
421 study. A vertical positive correlation between Nb# and Mn content is observed in these micas
422 (Figure 9b).

423 *Vein micas*: As seen in Figures 9a and 9c, the first (Fe-Li-mca$_{1\text{-}I}$) and fourth (Fe-Li-mca$_{4\text{-}III}$)
424 generations of micas display positive correlations between Mn and W or Nb+Ta, the Fe-Li-
425 mca$_{4\text{-}III}$ being the most depleted. A group of Fe-Li-mca$_{1\text{-}I}$ analyses are displaced from the
426 overall trend and most likely represent the Fe-Li-mca$_{4\text{-}III}$ overgrowth (Z1 to Z4, Figure 7) and,
427 indeed, these micas plot with the Fe-Li-mca$_{4\text{-}III}$ micas in all diagrams. In contrast, the Fe-Li-
428 mca$_{2\text{-}I}$ micas plot as a cluster in all diagrams (Figures 9a, c and d). Compared to other
429 generations of micas, the Fe-Li-mca$_{2\text{-}I}$ micas are the most W-enriched (20 to 30 ppm),
430 whereas the Fe-Li-mca$_{1\text{-}I}$ micas are distinguished by higher Nb+Ta (up to 1.4 ppm). The Fe-
431 Li-mca$_{4\text{-}III}$ micas are characterized by elevated Sn contents (up to 820 ppm) and very low W
432 and Nb+Ta values. Due to the LA-ICPMS spot size, Fe-Li-mca$_{3\text{-}I}$ micas could not be analysed
433 for trace element contents.

Greisen micas: Compared to the micas analysed in veins, the greisen micas are enriched in Nb and Ta (Figure 9a) and exhibit constant (close to the granite average) Nb# (Figure 9b). In Figure 8a and b, the greisen micas also share some similarities with the stage I micas.

Composition of chlorites

A total of 33 EMPA analyses were performed on chlorites ($Chl_{1\text{-}II}$ and $Chl_{2\text{-}III}$) that crystallized in the veins in stages II and III. Analyses were carried out on homogeneous $Chl_{1\text{-}II}$ and 100-µm size spherolites of $Chl_{2\text{-}III}$, perpendicular to their Fe-Mg zonation (Table 3, Figure 10). All of these chlorites were found to be tri/dioctahedral Fe–chlorites with compositions that lie between ripidolite-brunsvigite and pycnochlorite fields. In the Al^{IV} versus Al^{VI} plot, both generations of chlorite are displaced from the Tschermak line, which is always the case for low-temperature chlorites (Figure 10c; Cathelineau and Nieva, 1985). The $Chl_{2\text{-}III}$ chlorites present FeO contents of 17 to 35%, with Fe/(Fe+Mg) ratios of 0.3 to 0.8 (Table 3). From the core to the margin of the spherolites, major elements, especially FeO and MgO concentrations, show oscillatory variations (Figure 10a and b), but no general trend can be distinguished.

Temperatures were calculated using the graphical geothermometer of Cathelineau and Bourdelle (2015) and plotted in the Si-R^{2+} diagram of Wiewiora and Weiss (1990) (Figure 10d). This thermometer is based on the chlorite-quartz equilibrium. It does not require prior knowledge of the valence state of iron and is calibrated for low-T chlorites (T<350°C and pressures below 4kbar). The temperatures obtained range from 180 to 260°C for $Chl_{1\text{-}II}$ (average temperature of 200°C) and 200 to 380°C for $Chl_{2\text{-}III}$ (average temperature of 300°C) and correspond to temperatures reached during the second and third stages of crystallization

of the veins. No correlation between the calculated temperatures and the petrographic zoning in the $Chl_{2\text{-III}}$ or chemical composition was observed.

Discussion

Major elements in hydrothermal micas: evidence for fluid mixing

Fe-Li-mca$_{1,2\text{-I}}$ micas: In the Al-Si-R^{2+} diagram (Figure 8), the early Fe-Li-mca$_{1,2\text{-I}}$ display two trends: a "phlogopite-zinnwaldite" trend between two poles **a** and **b**, and a "zinnwaldite-muscovite" trend between the same **b** pole and a muscovite **c** pole (Figure 8b).

The systematic alternation between zinnwaldite and muscovite compositions during the growth of Fe-Li-mca$_{1,2\text{-I}}$ indicates the coexistence, at this time in the Piaotang hydrothermal system, of three distinct hydrothermal fluids responsible for the **a-b** and **b-c** trends. The **b-c** trend may be interpreted as a mixing trend between two fluids, one richer in Fe and Mg and the other, richer in Al, that co-precipitate in either Fe-Li-mca$_{1\text{-I}}$ or Fe-Li-mca$_{2\text{-I}}$. By contrast, the zinnwalditic **a-b** trend can be interpreted in terms of closed system crystallization (correlated Fe and Mg contents). The **a**-pole is in fact associated with a primitive fluid end-member (F_A), whereas the **b**-pole is associated with the evolution of F_A towards a F_B composition by fractional crystallization (closed system). Moreover, the **b-c** trend might be interpreted to be the result of an opening of the system, with the arrival of a new F_C fluid end-member (associated with the **c**-pole), and a mixing of F_C with the residual F_B fluid. This trend is also observed in the greisen micas (**g-h** trend). According to this interpretation, the complex structure of the Fe-Li-mca$_{1,2\text{-I}}$ would result in a combination of alternating influxes of F_A and F_C, with repeated periods of closure of the system, allowing the evolution of F_A into F_B. This is consistent with the continuous presence of tectonic activity recorded during the

hydrothermal process and the repetitive occurrence of crack-seal phenomena. These early micas share similar compositions and processes with early micas observed in the mineralizing stage of the Maoping deposit (also from the Dayu district) by Legros et al. (2016).

Fe-Li-mca$_{3\text{-}I}$: The late stage I micas, either zinnwaldite, or Li-Fe-ms, display similar trends to the other Piaotang micas (Figure 8b). The same pattern of a double trend converging towards the same mica composition is observed. Fe-Li-mca$_{3\text{-}I}$ are therefore likely to result from the same combination of closed system crystallization and mixing as the Fe-Li-mca$_{1,2\text{-}I}$ micas.

Fe-Li-mca$_{4\text{-}III}$: The Fe-Li-mca$_{4\text{-}III}$ display a single trend between a zinnwalditic **d** pole and a muscovite **e** pole (Figure 8c), consistent with a scheme of fluid mixing between the two end-members. Direct evidence for mixing is found in zoned overgrowths at the microscopic scale, where compositional changes could not be caused by a fractional crystallization (closed system) process (i.e., either Fe and Mg co-vary or Fe decreases when Mg increases) (Figure 7). The consistency between these **d** and **e** poles and the previous **b** and **c** poles will be addressed in the following sections. These post-mineralization micas are similar in composition to micas observed in the post-mineralizing stages of the Maoping deposit (also from the Dayu district) (Legros et al. 2016).

Conditions of interpretation of trace element compositions

The chemical composition of a given hydrothermal mineral is a record of the fluid composition, generally controlled by the partition coefficients of the incorporated elements between the mineral and the fluid. These are in turn controlled by crystal chemistry constraints and intensive parameters (P, T, pH, fO_2, etc.). Crystal chemistry constraints are clear for major elements, and may also be significant for trace elements. For instance,

incorporation of Li (likewise Nb and Ta) in trioctahedral micas depends on Al, due to the $Li_{+1}(Fe, Mg)_{+1}Al_{-1}$ mechanism of incorporation. In the same way, Sn and W are incorporated by exchanges involving Ti (and also Fe, Mg in the case of W) (Bos, 1990). Generally speaking, crystal chemistry constraints are not well established for most trace elements in micas. Nevertheless, it may be suggested that, at the 1000 ppm level (and below), the ability of sites and the major elements needed for the substitution mechanisms are always sufficient to allow element incorporation. In this respect, the presence, or not, of a given trace element in a mica, is only governed by the presence of the element in the hydrothermal fluid. The abundance of the element in the mica is however controlled by the fluid-to-mica partition coefficient of the element, and under a given set of intensive parameters, significant differences between the partition coefficients of distinct trace elements might exist.

Experimental data related to mica-fluid partition coefficients are scarce and very limited for hydrothermal conditions, experiments usually being conducted at high temperature (over 500°C). For instance, concerning F entry into micas, Zhu and Sverjensky (1991) conclude that the higher the temperature, the lower the amount of fluorine that partitions into minerals. In contrast, following the experimental results of Munoz and Ludington (1977), the F/(F+OH) ratio of muscovite and phlogopite correlates positively with temperature (but only significantly at $T > 500$°C). According to Munoz and Ludington (1977), when muscovite equilibrates with biotite, it is systematically poorer in fluorine with no dependence upon octahedral occupancy (i.e., the Al content). Nevertheless, both Li and Mg should increase F partitioning in muscovite. Experiments on Rb and Cs partitioning between phlogopite and fluid performed at 800°C and 0.2 to 4 GPa by Melzer and Wunder (2001) show that while Rb partitions in the mineral, Cs partitions into the fluid. Thus, the Rb/Cs ratio in phlogopite is not representative of the fluid composition. However, from experiments on phlogopite at 650°C and 0.2 GPa, Bos (1990) concluded that the Rb, Zn, Pb and Cu contents of the mica are only

532 controlled by their concentrations in the fluid. From these limited data, it may be estimated
533 that the main control on the incorporation of elements into a mica structure, is their abundance
534 in the hydrothermal fluids, and that their ratios in the mineral should therefore be close to
535 their ratios in the fluids. The large compositional differences between the different Piaotang
536 mica generations may thus be safely interpreted in terms of differences in the hydrothermal
537 fluid compositions.

538

539 **Trace elements: characterization of fluid end-members**

540

541 The data obtained from the Fe-Li-mca$_{1\text{-}I}$ and Fe-Li-mca$_{2\text{-}I}$ micas represent combinations of
542 both the **a-b** and **b-c** trends, depending on the local proportion of zinnwaldite and Fe-Li-ms
543 components at the spot site. Considering the mica structures, it seems that the Fe-Li-ms
544 components are statistically more abundant in the Fe-Li-mca$_{1\text{-}I}$ micas, which should
545 consequently yield more information on the **b-c** trend. Conversely, in the Fe-Li-mca$_{2\text{-}I}$
546 structure, the zinnwaldite and Fe-Li-ms components are more equally distributed and are
547 more likely representative of the **b** pole. The data in Figure 8b are quite consistent with these
548 suggestions: the Fe-Li-mca$_{1\text{-}I}$ micas lie along trends suggestive of mixing, whereas the Fe-Li-
549 mca$_{2\text{-}I}$ data plot in a more homogeneous cluster, likely representing an average composition.

550 Given the trace element data for these micas, it is possible to simplify our interpretation with a
551 two-fluid model. Indeed, all hydrothermal mica generations (Fe-Li-mca$_{1\text{-}I}$, Fe-Li-mca$_{2\text{-}I}$, Fe-
552 Li-mca$_{4\text{-}III}$ and greisen) are characterized by trends in the trace element diagrams (Figure 9).
553 According to major element interpretations, these trends may be considered as reflecting
554 mixing events and therefore may define four pairs of potential end-members (**a** and **b** for Fe-
555 Li-mca$_{1\text{-}I}$, **c** and **d** for Fe-Li-mca$_{2\text{-}I}$, **e** and **f** for Fe-Li-mca$_{4\text{-}III}$, and **g** and **h** for greisen micas)

(Figure 9e and f). Owing to the fact that Mn is more abundant in zinnwaldite and other Fe-rich micas, and in reference to the W-Mn diagram (Figure 9c), **a** and **c** correspond to the F_B end-member while **b** and **d**, reflect the F_C end-member. The W-Ba and Sn-Ba diagrams allows us to refine our interpretation of the trace element data. It appears (Figure 9e and f) that two series of end-members (**g**, **a**, **f** and **h**, **d**, **b**, respectively) display well-defined trends, connecting the earliest vein micas to the greisen micas. In contrast, the later Fe-Li-mca$_{4\text{-III}}$ micas form their own trend and result from the F_E-F_F mixing process. Following this logic, the greisen micas appear to result from the interaction of two series of fluids associated with the stage I micas (F_B and F_C). These fluids evolve from a metal-poor to a metal-rich composition with a constant fractionation *vs* mixing model (see section above).

Relationships with the ore-forming process

Given that both the F_B and F_C fluids carry significant concentrations of metal, both are potentially able to contribute to the ore-forming process. However, micas precipitating from the mixing ore-depositing fluid record a lower saturation value than micas from the pre-mixing stages. Thus, micas from the ore-stage are expected to be depleted in rare metals. This may explain, for instance, why the Fe-Li-mca$_{1\text{-I}}$ micas are depleted in W (coeval with wolframite) and the Fe-Li-mca$_{2\text{-I}}$ micas are depleted in Sn (coeval with cassiterite). Correlatively, the relative enrichment in Nb in the Fe-Li-mca$_{1\text{-I}}$ micas could result from the incompatible character of Nb, which was also not detected at a significant level in wolframite or in cassiterite, whereas other vein micas would be very Nb-poor. Therefore, the Fe-Li-mca$_{2\text{-I}}$ micas and the greisen micas have recorded a period where the conditions for ore-deposition were not encountered. Moreover, greisen micas are considered to be the result of the biotite granite transformation, which includes alteration of the initial Nb-Ta-rich biotite into an

581 enriched Fe-Li muscovite in the greisen with inherited rare metals. This interpretation is
582 supported by the constant Nb# in greisen micas, fixed at the average value of the biotite
583 precursors. In their study of the Dajishan deposit, Wu et al. (2017) observed that the
584 muscovite in RMG granites was enriched in Nb, Ta, Rb and Cs relative to the vein-hosted
585 muscovite, whereas both displayed similar Sn and W contents (similar to the Piaotang case).
586 In Wu et al. (2017), muscovites in the granite were interpreted to have formed by the same
587 fluids that formed the veins but modified through reaction with the HFSE-enriched granite in
588 the same way as in the Piaotang deposit. The lower Nb and Ta contents in the greisen micas
589 relative to the granite micas reflect the leaching of these rare metals out from the granite body.

590 The late Fe-Li-$mca_{4\text{-III}}$ micas, which were deposited at the very beginning of stage III,
591 characterized by renewed Sn deposition (abundant $Stn_{1\text{-III}}$ and minor $Cst_{3\text{-III}}$), are enriched in
592 Sn and depleted in W, and may thus be considered as having recorded a Sn-rich fluid, which
593 would, in this case, be identified as the F_F end-member (Figure 9b and f).

594

595 **Comparison with published fluid inclusion studies**

596

597 Fluid inclusion (FI) studies were performed at the Piaotang deposit on quartz (Wang et al.
598 2013b; Ni et al. 2015), cassiterite (Zeng et al. 2002; Wang et al. 2013b) and wolframite (by
599 infrared microscopy; Ni et al. 2015). The corresponding data are summarized in Figure 11.
600 For each mineral presented in Figure 11, the primary FI were plotted. Secondary inclusions
601 were only analysed in quartz by Ni et al. (2015) and are referred to as "post stage I". The FI
602 display a trend of decreasing temperature from wolframite (400 to 300°C) to cassiterite (350
603 to 300°C) and finally to post-ore fluids trapped in quartz (300 to 150°C). Fluid mixing is
604 attested to by salinity variations in wolframite (between 4.6 and 8.9 wt. % eq. NaCl) and

quartz (0 to 11 wt. % eq. NaCl), whereas cassiterite trapped the most saline fluids (8.5 to 9.5 wt. % eq. NaCl).

The preceding interpretations of mica compositions are consistent with these results. Moreover, the decrease in temperature revealed by the FI studies would explain why the Fe-Li-mca$_{2\text{-I}}$ micas are not associated with wolframite deposition in that the temperature decrease could have inhibited wolframite precipitation.

Origin of the fluids

Stage I fluids: As discussed in the preceding sections, the F_B fluid, or, more precisely, its F_A parent, are likely to be representative of the ore-forming fluids at stage I. The interpretative model detailed in the previous section implies that each F_B^x should be associated with an F_A^x fluid (Figure 9) involving a renewal of the source. According to the major and trace element composition data, (except for their W (and Sn) content) the F_A fluids are characterized by high contents of F, Fe+Mg (Fe# of 0.75) and Mn. Such characteristics could be interpreted as reflecting a magmatic-hydrothermal origin, involving a rare metal granite (RMG) with a high F content. However, such fluids are unlikely to be Mg-rich as they are associated with evolved granites. Moreover, the enrichment in F should be associated with Al enrichment. In any case, this RMG could not be the Piaotang granite. Interaction of an evolved granite with an external fluid, which (based on the Fe and Mg contents) could be of metamorphic origin, would be more likely. However, no volatile component was observed in the FI studies (Zeng et al. 2002; Wang et al. 2013b, Ni et al. 2015).

The F_C fluid, poorer in F, represents the diluting fluid recorded in the FI studies. Wang et al. (2009) characterize this fluid as a meteoric air-saturated fluid, interpreted to have recorded

downward infiltration of meteoric water through faults and fractures. This shallow water could have infiltrated through tectonically-activated regional drains. However, the trace element content of this F_c fluid, notably in terms of rare metals, suggests that this end-member equally interacted with the same granite as the F_A fluids.

Stage III fluids: The stage III F_E and F_F fluid end-members are interpreted in the same terms as the stage I end-members, with F_E being the Sn-rich ore-forming fluid (Figure 9f) and F_F, the external, diluting end-member.

Geothermometry implications

Fluid inclusion analyses have only been performed on stage I wolframite, quartz and cassiterite, as presented previously (Zeng et al., 2002, Wang et al., 2008, Ni et al., 2015). Chlorite geothermometry allows us to constrain post-mineralization temperatures at the Piaotang deposit. At the end of stage I, a brittle to ductile (based on microscopic observations only) environment is recorded (Figure 4). According to Stöckhert et al. (1999), the temperature of the brittle–plastic transition in quartz is between 310±30 and 350±50 °C. Cassiterite was the last of the three minerals to crystallize (Figure 4) and recorded homogenization temperatures of between 300 and 350°C (Zeng et al., 2002). Moreover, as fluids were circulating, a hydrostatic gradient should be considered in our system. Given this, even if a wide gradient of 30°C/km to 90°C/km is considered, the cassiterite crystallizing fluids should have been at higher temperatures (at least 400°C). Thus, the fluids must have been cooling at the end of stage I, supporting the idea of involvement of a meteoric fluid (Fc).

Stage II and III temperatures have not been constrained in the literature. However, scheelite ($Sch_{1\text{-}II}$) development at the expense of wolframite is usually interpreted as reflecting a

temperature decrease (Wood and Samson 2000). Moreover, $Chl_{1\text{-}II}$ compositions applied to the Cathelineau and Bourdelle (2015) geothermometer indicate that the Piaotang system cooled to a temperature of close to 200°C during stage II. Moreover, the $Chl_{2\text{-}III}$ geothermometer indicates that the hydrothermal fluids were reheated to a temperature of at least 300°C during stage III. The increase in temperature at this stage could explain the crystallization of new generations of cassiterite and wolframite.

Implications

A new paragenesis of the Piaotang deposit has been established here, composed of four stages of emplacement, three of which involve W-Sn minerals: (i) the "silicate-oxide" stage , which hosts the main mineralization; (ii) a "calcic" stage with scheelite and columbo-tantalite; (iii) a "base metal sulphides" stage with wolframite and cassiterite; and finally (iv) a late "sulphide" stage. This detailed paragenesis highlights for the first time the deposition of W-Sn minerals during three successive stages with a complementary Nb-Ta occurrence during the "calcic" stage.

Fe-Li-mica and chlorite are common in W-Sn deposits, which are usually emplaced during multiple magmatic and hydrothermal events that affect granites and other country rocks. In this work we have presented a detailed study of Fe-Li-mica and chlorites that can be correlated with fluid inclusion studies in order to observe diverse magmatic and hydrothermal influences. The correlation between the W-Sn content of Fe-Li-micas and its concordance with the crystallization of wolframite and cassiterite confirms that Li-micas are good tracers of mineralization in this kind of deposit.

Moreover, by correlating the geochemistry of micas and chlorite with the findings of previous fluid inclusion studies, it appears that two mixing end-members (magmatic and meteoric), clearly identified in both approaches, are associated with the deposition of wolframite and

cassiterite during the first stage. However, it should be noted that this study also highlights involvement of a third fluid (external and possibly metamorphic) during deposition of the mineralization and that the circulation of fluids during stage I is responsible for the greisenization. More importantly, the now buried Piaotang biotite granite cannot be the source of the mineralizing magmatic fluids and that the source should instead be linked to a more evolved RMG granite that has not yet been identified.

Finally, our study of Fe-Li-mica and chlorite in the post-mineralizing stages has allowed, for the first time, the different processes involved after the "silicate-oxide" stage to be constrained. A new source of heat was induced into the system during stage III, enabling the crystallization of new generations of minerals of economic interest (cassiterite and wolframite). A fluid inclusion study of the post-mineralizing stages could help to identify the fluid at the origin of this heat advection.

Acknowledgements

We are particularly indebted to Olivier Rouer, Lise Salsi, Andreï Lecomte, Chantal Peiffert and Sandrine Mathieu for their help during EPMA, LA-ICPMS and SEM data acquisition. This research was supported by the collaboration between Carnot ICEEL-Nancy and Carnot BRGM-Orléans. Access to the Piaotang deposit, and underground sampling was gratefully appreciated, particularly the assistance provided by Zeying Zhu, Xudong Che and local miners. RCW's research is supported by the NSF of China (Grant no. 41230315), and the MOE-SAFE Affairs of China joint "111" programme (Grant no. B13021). We are also grateful to Jindrich Kynicky and Marieke Van Lichtervelde for their constructive reviews that helped improve this manuscript.

703 **References**

704

705 Audétat, A., Gunther, D., and Heinrich, C.A. (1998) Formation of a magmatic-hydrothermal
706 ore deposit: insights with LA-ICPMS analysis of fluid inclusions. Science, 279, 2091.
707 Barton, Jr., P.B. (1978) Some ore textures involving sphalerite from the Furutobe mine, Akita
708 Prefecture, Japan. Mining Geology, 28, 293–300.
709 Beuchat, S., Moritz, R., and Pettke, T. (2004) Fluid evolution in the W–Cu–Zn–Pb San
710 Cristobal vein, Peru: fluid inclusion and stable isotope evidence. Chemical Geology,
711 210, 201-224.
712 Blamart, D. (1991) Les concentrations tungstifères et stannifères : caractérisation isotopique
713 des fluides minéralisateurs, sur l'exemple du gisement Sn-W de Walmès, 162 p. Ph.D.
714 thesis, INPL, Nancy.
715 Bortnikov, N.S., Genkin, A.D., Dobrovol'skaya, M.G., Muravitskaya, G.N., and Filimonova,
716 A.A. (1991) The nature of chalcopyrite inclusions in sphalerite; exsolution,
717 coprecipitation, or "disease"? Economic Geology, 86, 1070-1082.
718 Bos, A. (1990) Hydrothermal element distributions at high temperatures: an experimental
719 study on the partitioning of major and trace elements between phlogopite, haplogranitic
720 melt and vapour. 107p. Ph.D. thesis, Faculteit Aardwetenschappen.
721 Carruzzo, S., Kontak, D.J., Clarke, D.B., and Kyser, T.K. (2004) An integrated fluid–mineral
722 stable-isotope study of the granite-hosted mineral deposits of the New Ross area, south
723 mountain batholith, Nova Scotia, Canada: evidence for multiple reservoirs. The
724 Canadian Mineralogist, 42, 1425-1441.
725 Cathelineau, M., and Nieva, D. (1985) A chlorite solid solution geothermometer, the Los
726 Azufres (Mexico) geothermal system. Contributions to Mineralogy and Petrology, 91,
727 235-244.

728 Charvet, J. (2013) The Neoproterozoic-Early Paleozoic tectonic evolution of the South China
729 Block: an overview. Journal of Asian Earth Sciences, 74, 198-209.
730 Charvet J., Shu L-S., Faure M., Choulet F., Wang B., Lu H-F., and Le Breton N. (2010)
731 Structural development of the Lower Palaeozoic belt of South China: genesis of an
732 intracontinental orogeny. Journal of Asian Earth Sciences, 39, 309-330.
733 Chicharro, E., Boiron, M.C., Lopez-Garcia, J.A., Barfod, D.N., and Villaseca, C. (2016)
734 Origin, ore forming fluid evolution and timing of the Logrosan Sn-(W) ore deposits
735 (Central Iberian Zone, Spain). Ore Geology Reviews, 72, 896-913.
736 Costi, H.T., Dall'Agnol, R., Borges, R.M.K., Minuzzi, O.R.R., and Teixeira, J.T. (2002) Tin-
737 bearing sodic episyenites associated with the Proterozoic A-type Agua Boa granite,
738 Pitinga Mine, Amazonian Craton, Brazil. Gondwana Research, 5, 435-451.
739 Faure, M., Sun, Y., Shu, L., Monie, P., and Charvet, J. (1996) Extensional tectonics within a
740 subduction-type orogen. The case study of the Wugongshan dome (Jiangxi Province,
741 southeastern China). Tectonophysics, 263, 77-106.
742 Foster, M.D. (1960) Interpretation of the composition of lithium micas. U.S. Geological
743 Survey Professional Paper, 354-E, 115-47.
744 Foster, M.D. (1962) Interpretation of the composition and a classification of the chlorites.
745 U.S. Geological Survey Professional Paper, 414-A, 1-33.
746 Giuliani, G. (1985) Le gisement de tungstène de Xihuashan (Sud-Jiangxi, Chine): Relations
747 granites, alterations deutériques-hydrothermales, minéralisations. Mineralium
748 Deposita, 20, 107-115.
749 Günther, D., Frischknecht, R., Heinrich, C.A., and Kahlert, H.J. (1997) Capabilities of an
750 argon fluoride 193 nm excimer laser for laser ablation inductively coupled plasma
751 mass spectrometry microanalysis of geological materials. Journal of Analytical
752 Atomic Spectrometry, 12, 939–944.

He, Z., Xu, X., Zou, H., Wang, X., and Yu, Y. (2010) Geochronology, petrogenesis and metallogeny of Piaotang granitoids in the tungsten deposit region of South China. Geochemical Journal, 44, 299-313.

Hua, R., Chen, P., Zhang, W., and Lu, J. (2005) Three large-scale metallogenic events related to the Yanshanian Period in Southern China. In: Mineral Deposit Research: Meeting the Global Challenge. Springer Berlin, Heidelberg, 401-404.

Hu, R.Z., and Zhou, M.F. (2012) Multiple mesozoic mineralization events in South China - an introduction to the thematic issue. Mineralium Deposita, 47, 579-588.

Jochum, K.P., Weis, U., Stoll, B., Kuzmin, D., Yang, Q., Raczek, I., Jacob, D.E., Stracke, A., Birbaum, K., Frick, D.A., Gunther, D., and Enzweiler, J. (2011) Determination of reference values for NIST SRM 610-617 glasses following ISO guidelines. Geostandards and Geoanalytical Research, 35, 397-429.

Johan, Z., Strnad, L., and Johan, V. (2012) Evolution of the Cinovec (Zinnwald) granite cupola, Czech Republic: Composition of feldspars and micas, a clue to the origin of W, Sn mineralization. The Canadian Mineralogist, 50, 1131-1148.

Kamenetsky, V.S., Naumov, V.B., Davidson, P., Van Achtenbergh, E., and Ryan, C.G. (2004) Immiscibility between silicate magmas and aqueous fluids: a melt inclusion pursuit into the magmatic-hydrothermal transition in the Omsukchan Granite (NE Russia). Chemical Geology, 210, 73-90.

Lach, P., Mercadier, J., Dubessy, J., Boiron, M.C., and Cuney, M. (2013) In situ quantitative measurement of rare earth elements in uranium oxides by laser ablation-inductively coupled plasma-mass spectrometry. Geostandards and Geoanalytical Results, 37, 1-20.

Legros, H., Marignac, C., Mercadier, J., Cuney, M., Richard, A., Wang, R-C., Charles, N., and Lespinasse, M-Y. (2016) Detailed paragenesis and Li-mica compositions as

777 recorders of the magmatic-hydrothermal evolution of the Maoping W-Sn deposit
778 (Jiangxi, China). Lithos, 264, 108-124.
779 Leisen, M., Boiron, M.C., Richard, A., and Dubessy, J. (2012) Determination of Cl and Br
780 concentrations in individual fluid inclusions by combining microthermometry and LA-
781 ICPMS analysis: Implications for the origin of salinity in crustal fluids. Chemical
782 geology, 330-331, 197-206.
783 Li, X.H., Li, W.X., Li, Z.X., Lo, C.H., Wang, J., Ye, M.F., and Yang, Y. H. (2009)
784 Amalgamation between the Yangtze and Cathaysia Blocks in South China: constraints
785 from SHRIMP U–Pb zircon ages, geochemistry and Nd–Hf isotopes of the Shuangxiwu
786 volcanic rocks. Precambrian Research, 174, 117-128.
787 Li, H., Zhang, H., Ling, M. X., Wang, F. Y., Ding, X., Zhou, J. B., and Sun, W. (2011)
788 Geochemical and zircon U–Pb study of the Huangmeijian A-type granite: implications
789 for geological evolution of the Lower Yangtze River belt. International Geology
790 Review, 53, 499-525.
791 Li, J.H., Zhang, Y.Q., Dong, S.W., and Johnson, S.T. (2014) Cretaceous tectonic evolution of
792 South China: a preliminary synthesis. Earth Science reviews, 134, 98-136.
793 Liu, R., Zhou, H., Zhang, L., Zhong, Z., Zeng, W., Xiang, H., and Li, C. (2010) Zircon U–Pb
794 ages and Hf isotope compositions of the Mayuan migmatite complex, NW Fujian
795 Province, Southeast China: constraints on the timing and nature of a regional
796 tectonothermal event associated with the Caledonian orogeny. Lithos, 119, 163-180.
797 Liu, Q., Yu, J.H.,Wang, Q., Su, B., Zhou, M.F., Xu, H., and Cui, X. (2012) Ages and
798 geochemistry of granites in the Pingtan-Dongshan metamorphic belt, coastal South
799 China: new constraints on Late Mesozoic magmatic evolution. Lithos, 150, 268–286.

800 Longerich, H.P., Günther, D., and Jackson, S.E. (1996) Elemental fractionation in laser
801 ablation inductively coupled plasma mass spectrometry. Fresenius' journal of
802 analytical chemistry, 355, 538-542.
803 Mao, Z., Cheng, Y., Liu, J., Yuan, S., Wu, S., Xiang, X., and Luo, X. (2013) Geology and
804 molybdenite Re-Os age of the Dahutang granite-related veinlets-disseminated tungsten
805 ore field in the Jiangxi Province, China. Ore Geology Reviews, 53, 422-433.
806 Marignac, C., and Cathelineau, M. (2009) The nature of ore-forming fluids in peri-batholitic
807 Sn-W deposits and a classification. SGA congress abstract.
808 Melzer, S., and Wunder, B. (2001) K–Rb–Cs partitioning between phlogopite and fluid:
809 experiments and consequences for the LILE signatures of island arc basalts. Lithos,
810 59, 69-90.
811 Monier, G., and Robert, J.L (1986) Evolution of the miscibility gap between muscovite and
812 biotite solid solutions with increasing lithium content: an experimental study in the
813 system K_2O-Li_2O-MgO-FeO-Al_2O_3-SiO_2-H_2O-HF at 600°C, 2kbar PH_2O: comparison
814 with natural lithium micas. Mineralogical magazine, 50, 641-651.
815 Munoz, J. L., and Ludington, S. (1977) Fluorine-hydroxyl exchange in synthetic muscovite
816 and its application to muscovite-biotite assemblages. American Mineralogist, 62, 304-
817 308.
818 Ni, P., Wang, X.D., Wang, G.G., Huang, J.B., Pan, J.Y., and Wang, T.G. (2015) An infrared
819 microthermometric study of fluid inclusions in coexisting quartz and wolframite from
820 Late Mesozoic tungsten deposits in the Gannan metallogenic belt, South China. Ore
821 Geology Reviews, 65, 1062–1077.
822 Neiva, A.M.R. (2013) Micas, feldspars and columbite–tantalite minerals from the zoned
823 granitic lepidolite-subtype pegmatite at Namivo, Alto Ligonha, Mozambique.
824 European Journal of Mineralogy, 25, 967-985.

825 Paton, C., Hellstrom, J., Paul, B., Woodhead, J., and Hergt, J. (2011) Iolite: Freeware for the
826 visualization and processing of mass spectrometric data. Journal of Analytical Atomic
827 Spectometry, 26, 2508.
828 Shu, L., Faure, M., Wang, B., Zhou, X., and Song, B. (2008) Late Palaeozoic–Early Mesozoic
829 geological features of South China: response to the Indosinian collision events in
830 Southeast Asia. Comptes Rendus Geoscience, 340, 151-165.
831 Shu, L.S., Zhou, X.M., Deng, P., Wang, B., Jiang, S.Y., Yu, J.H., and Zhao, X.X. (2009)
832 Mesozoic tectonic evolution of the Southeast China Block: new insights from basin
833 analysis. Journal of Asian Earth Sciences, 34, 376–391.
834 Smith, M., Banks, D.A., Yardley, B.W.D., and Boyce, A. (1996) Fluid inclusion and stable
835 isotope constraints on the genesis of the Cligga Head Sn-W deposit, S.W. England.
836 European Journal of Mineralogy, 8, 961-974.
837 Stöckhert, B., Brix, M. R., Kleinschrodt, R., Hurford, A. J., and Wirth, R. (1999)
838 Thermochronometry and microstructures of quartz—a comparison with experimental
839 flow laws and predictions on the temperature of the brittle–plastic transition. Journal of
840 Structural Geology, 21, 351-369.
841 Tanelli, G. (1982) Geological setting, mineralogy and genesis of tungsten mineralization in
842 Dayu district, Jiangxi (People's Republic of China): an outline. Mineralium Deposita,
843 17, 279–294.
844 Tischendorff, G., Gottesmann, B., Forster, H.J., and Trumbull, R.B. (1997) On Li-bearing
845 micas: estimating Li from electron microprobe analyses and an improved diagram for
846 graphical representation. Mineralogical magazine, 61, 809-834.
847 Thomas, R., Förster, H.J., Rickers, K., and Webster, J. (2005) Formation of extremely F-rich
848 hydrous melt fractions and hydrothermal fluids during differentiation of highly

849 evolved tin-granite magmas: a melt-fluid inclusion study. Contributions to Mineralogy
850 and Petrology, 148, 582-641.
851 USGS, 2016. Tungsten. Mineral Commodity Summaries. 180-181.
852 Walsche, J.L. (1986) A six-component chlorite solid solution model and the conditions of
853 chlorite formation in hydrothermal and geothermal systems. Economic Geology, 81,
854 681-703.
855 Wang, D.Z., Shu, L.S., Faure, M., and Sheng, W.Z. (2001) Mesozoic magmatism and granitic
856 dome in the Wugongshan Massif, Jiangxi province and their genetical relationship to
857 the tectonic events in southeast China. Tectonophysics, 339, 259-277.
858 Wang, Z. Q., Yin, C. Y., Gao, L. Z., Tang, F., Liu, Y. Q., and Liu, P. J. (2006) The character
859 of the chemical index of alteration and discussion of subdivision and correlation of the
860 Nanhua System in Yichang area. Geological Review, 52, 577-585.
861 Wang, X-D., Ni, P., Jiang, S-Y., Zhao, K-D., and Wang, T-G. (2009) Origin of ore-forming
862 fluid in the Piaotang tungsten deposit in Jiangxi Province: Evidence from helium and
863 argon isotopes. Chinese Science Bulletin, 55, p. 628-634.
864 Wang, Y., Zhang, A., Fan, W., Zhao, G., Zhang, G., Zhang, Y., and Li, S. (2011) Kwangsian
865 crustal anatexis within the eastern South China Block: geochemical, zircon U–Pb
866 geochronological and Hf isotopic fingerprints from the gneissoid granites of Wugong
867 and Wuyi–Yunkai Domains. Lithos, 127, 239-260.
868 Wang, X-D., Ni, P., Yuan, S-D., and Wu, S-H. (2013b) Fluid inclusion studies on coexisting
869 cassiterite and quartz from the Piaotang tungsten deposit, Jiangxi Province, China. Acta
870 Geologica Sinica, 87, 850–859 In Chinese with English abstract.
871 Wang, Y-J., Fan, W-M., Zhang, G-W., and Zhang, Y-H. (2013) Phanerozoic tectonics of the
872 South China Block: key observations and controversies. Gondwana Research, 23, 1273-
873 1305.

874 Wang, X., Chen, J., and Ren, M. (2016) Hydrothermal zircon geochronology: age constraint
875 on Nanling range tungsten mineralization (Southeast China). Ore geology reviews, 74,
876 63-75.
877 Wei, W., Hu, R., Bi, X., Peng, J., Su, W., Song, S., and Shi, S. (2012). Infrared
878 microthermometric and stable isotopic study of fluid inclusions in wolframite at the
879 Xihuashan tungsten deposit, Jiangxi province, China. Mineralium Deposita, 47, 589-
880 605.
881 Wiewióra, A., and Weiss, Z. (1990) Crystallochemical classifications of phyllosilicates based
882 on the unified system of projection of chemical composition: II. The chlorite group.
883 Clay Minerals, 25, 83-92.
884 Wilkinson, J.J. (1990) The role of metamorphic fluids in the development of the Cornubian
885 Orefield: fluid inclusion evidence from south Cornwall. Mineralogical Magazine, 54,
886 219–230.
887 Wood, S., and Samson, I. (2000) The hydrothermal geochemistry of tungsten in granitoid
888 environments: I. Relative solubilites of ferbérite and scheelite as a function of T, P, pH,
889 and mNaCl. Economic Geology, 95, 43-182.
890 Wu, M., Samson, I. M., and Zhang, D. (2017) Textural and Chemical Constraints on the
891 Formation of Disseminated Granite-hosted W-Ta-Nb Mineralization at the Dajishan
892 Deposit, Nanling Range, Southeastern China. Economic Geology, 112, 855-887.
893 Xia, Y., Xu, X.S., Zou, H.B., and Liu, L. (2014) Early Paleozoic crust-mantle interaction and
894 lithosphere delamination in South China Block: evidence from geochronology,
895 geochemistry, and Sr-Nd-Hf isotopes of granites. Lithos, 184-187, 416-435.
896 Yao, J., Shu, L., Santosh, M., and Li, J. (2013) Geochronology and Hf isotope of detrital
897 zircons from Precambrian sequences in the eastern Jiangnan Orogen: Constraining the

898 assembly of Yangtze and Cathaysia Blocks in South China. Journal of Asian Earth
899 Sciences, 74, 225-243.
900 Zeng, Y., Liu, J., and Zhu, Y. (2002) Short-chain carboxylates in high-temperature ore fluids
901 of W-Sn deposits in south China. Geochemical Journal, 36, p. 219-234.
902 Zhang, C. L., Li, H. K., Santosh, M., Li, Z. X., Zou, H. B., Wang, H., and Ye, H. (2012)
903 Precambrian evolution and cratonization of the Tarim Block, NW China: Petrology,
904 geochemistry, Nd-isotopes and U–Pb zircon geochronology from Archaean gabbro-
905 TTG–potassic granite suite and Paleoproterozoic metamorphic belt. Journal of Asian
906 Earth Sciences, 47, 5-20.
907 Zhang, R., Lu, J., Lehmann, B., Li, C., Li, G., Zhang, L., and Sun, W. (2017) Combined
908 zircon and cassiterite U–Pb dating of the Piaotang granite-related tungsten–tin deposit,
909 southern Jiangxi tungsten district, China. Ore Geology Reviews, 82, 268-284.
910 Zhao, K.D., and Jiang, S.Y. (2004) Mineral chemistry of the Qitianling granitoid and the
911 Furong tin ore deposit in Hunan province, south China: Implications for the genesis of
912 granite and related tin mineralization. EMPGX Symposium Abstract, Lithos, 73, S124.
913 Zhao, W.W., Zhou, M.F., Li, Y.H.M., Zhao, Z., and Gao, J.F. (2017) Genetic types,
914 mineralization styles, and geodynamic settings of Mesozoic tungsten deposits in South
915 China. Journal of Asian Earth Sciences, 137, 109-140.
916 Zhou, T., Goldfarb, R.J., and Philips, G.N. (2002) Tectonics and distribution of gold deposits
917 in China – an overview. Mineralium Deposita, 37, 249–282.
918 Zhu, C., and Sverjensky, D.A. (1991) Partitioning of F-Cl-OH between minerals and
919 hydrothermal fluids. Geochimica et Cosmochimica Acta, 55, 1837-1858.
920

921 **Figure captions**

922

Figure 1: (**a**) Ore mining districts and metal deposits of the Cathaysia Block, (**b**) Detailed map of the southern part of the Jiangxi Province, SE China, showing the distribution of Jurassic and Cretaceous granitoids. The Piaotang deposit is located in the Dayu district in the south-western part of the Jiangxi province (Modified after Legros et al. (2016) and references therein).

Figure 2: Simplified geological map (**a**) and cross-section with associated strikes (**b**) of the Piaotang W-Sn deposit, showing the relationships between the deep granite, Cambrian host rocks, and mineralized veins and the sampling levels ((**a**) modified after Tanelli 1982 and (**b**) modified after Ni et al., 2015).

Figure 3: Mineralized veins as observed in the mine galleries at different levels of sampling. (**a**) Wolframite-cassiterite-quartz vein. (**b**) Fluorite-cassiterite-quartz vein. (**c**) Accumulated sulphides in the vein. (**d**) Fluorite accumulation in the vein.

Figure 4: Paragenetic sequence of veins in the Piaotang W–Sn deposit based on petrographic observations of samples from mine galleries at levels 268, 388 and 556. See text for details of the different stages, mineral abbreviations and notations.

Figure 5: Microphotographs of the mineralogical textures and associations of the Piaotang deposit. (**a**) Micrograined-granite with porphyritic feldspar and biotite (crossed polars). (**b**) Slightly deformed quartz grains and corroded muscovite from the greisen (crossed polars). Thin-section in (**c**) natural light and (**d**) crossed polars of the main minerals that crystallized in stage I ($Cst_{1\text{-}I}$, $Wf_{1\text{-}I}$, $Qtz_{1\text{-}I}$ and Fe-Li-mca), showing the multiple crack-seal episodes observed in quartz and wolframite. Abbreviations

948 according to the IMA: Ab = albite; Cst = cassiterite; Mca = micas; Or = orthoclase;
949 Qtz = quartz; Wf = wolframite.
950
951 Figure 6: Microphotographs of the mineralogical textures and associations of the Piaotang
952 deposit. (**a**) Alteration of $Wf_{1\text{-}I}$ into $Sch_{1\text{-}I}$ followed by the crystallization of
953 associated $Chl_{1\text{-}II}$, $Fl_{1\text{-}II}$ and $Clb_{1\text{-}II}$ during stage II (SEM). (**b**) Textures of stage II
954 retromorphosis of wolframite into scheelite associated with early stage I minerals
955 (crossed polars). (**c**) Alteration of early stage I $Toz_{1\text{-}I}$ by Fe-Li-$mca_{4\text{-}III}$ in stage III
956 (crossed polars). (**d**) Spherulites of chlorite that crystallized during the stage II
957 (SEM). (**e**) Microcracks lining the $Ccp_{1\text{-}IV}$ boundary with inclusions of $Cst_{3\text{-}III}$, $Wf_{2\text{-}}$
958 $_{III}$, $Stn_{1\text{-}III,}$ and symplectic textures observed between $Ccp_{1\text{-}III}$, $Sp_{1\text{-}III}$ and $Stn_{1\text{-}III}$
959 (SEM). (**f**) Association of the second generation of $Wf_{2\text{-}III}$ with $Fl_{2\text{-}III}$ and Fe-Li-$mca_{4\text{-}}$
960 $_{III}$ in stage III (SEM). (**g**) Association of a third generation of cassiterite $Cst_{3\text{-}III}$ and
961 $Stn_{1\text{-}III}$ to stage IV sulphides (SEM) replacing second stage chlorite $Chl_{1\text{-}II}$. (**h**)
962 Texture and association of $Ccp_{1\text{-}III}$, $Sp_{1\text{-}III,}$ $Gln_{1\text{-}IV,}$ $Bmt_{1\text{-}IV}$, $Bi_{1\text{-}IV}$ in stage IV (SEM).
963 Abbreviations according to the IMA: Bi = native bismuth; Bmt = bismuthinite; Ccp
964 = chalcopyrite; Chl = chlorite; Clb = Colombo-tantalite; Cst = cassiterite; Fl =
965 fluorite; Gln = galena; Mca = micas; Mlb = molybdenite; Py = pyrite; Qtz = quartz;
966 Sch = scheelite; Sp = sphalerite; Stn = stannite Toz = topaz; Wf = wolframite.
967
968 Figure 7: Detailed study of an altered Fe-Li-$mca_{1\text{-}I}$ spherolite into Fe-Li-$mca_{4\text{-}III}$. The chemical
969 profiles show the oscillatory changes in composition during alteration. All elements
970 are presented as apfu values, calculated from EPMA data.
971

Figure 8: Compositions of micas plotted on a Monier and Robert (1986) phase diagram as a function of R^{3+} (Al), R^{2+} (Fe+Mg+Mn) and Si (apfu). Each generation of micas from the veins, granite and greisen displays an evolution trend that can be described using end-member compositions from (a) to (h) and be compared to similar published data from the Maoping deposit (Legros et al., 2016). See discussion section for explanations.

Figure 9: Trace element binary diagrams for three generations of micas from the veins, the granite and the greisen in the Piaotang deposit (data from LA-ICPMS analysis). The chosen binary diagrams aim to unravel the behavior of different metals observed in trace amounts in micas and separate the evolution of each generation. "F_x^x" refer to fluids identified in the discussion section (see text for further explanation). The granite mica data have been removed from (**e**) and (**f**) binary diagrams for better visibility.

Figure 10: (**a**) Zoning in stage II chlorites and an example of the spatial distribution of analytical points across the zoning (SEM). (**b**) Compositional profiles corresponding to chemical variations in FeO and MgO along the transect shown in (**a**) (EMPA data). (**c**) Octahedral Al (apfu) vs. tetrahedral Al (apfu) in stage II and stage III chlorites (EMPA data). The line corresponds to the Tschermak line. (**d**) Distribution of temperature determined by chlorite graphical thermometry (Cathelineau and Bourdelle, 2015) and plotted in a T-R^{2+}-Si diagram.

Figure 11: Fluid inclusion data plotted on a binary salinity vs. homogenization temperature diagram after Ni et al., (2015), Wang et al., (2008) and Zeng et al., (2002).

This is a preprint, the final version is subject to change, of the American Mineralogist (MSA)
Cite as Authors (Year) Title. American Mineralogist, in press.
DOI: http://dx.doi.org/10.2138/am-2018-6196

997 **Table1. Selected major oxide contents from EPMA analyses and calculated structural formulae for micas from each stage, granite and greisen. Li_2O**
998 **contents were calculated using Tischendorff et al. (1997). Values preceded by the symbol '<' indicate element concentrations below the limit of**
999 **detection.**

EPMA (wt%)	**Fe-Li-mca$_{1\text{-}I}$ (N=54)**	**Fe-Li-mca$_{2\text{-}I}$ (N=13)**	**Fe-Li-mca$_{3\text{-}I}$ (N=26)**	**Fe-Li-mca$_{4\text{-}III}$ (N=26)**	**Granite (N=30)**	**Greisen (N=20)**
SiO_2	35.42	44.44	45.36	47.46	35.54	43.79
TiO_2	<0.05	0.06	<0.05	0.27	1.85	0.07
Al_2O_3	21.16	21.61	28.79	26.61	19.38	27.75
FeO	24.58	8.46	7.13	4.84	24.70	9.16
MnO	1.25	1.57	0.26	0.72	1.23	1.47
MgO	1.18	3.26	0.66	2.61	2.20	0.08
CaO	<0.07	<0.07	<0.07	<0.07	<0.07	<0.07
Na_2O	0.06	0.09	0.16	0.07	0.10	0.13
K_2O	9.59	10.77	10.65	9.83	8.89	8.93
Rb_2O	0.67	0.62	0.33	0.48	0.15	0.40
Li_2O *	2.07	4.68	2.87	2.54	2.11	2.40
F	2.24	6.91	1.82	4.07	0.73	2.02
O=F	1.12	3.45	0.91	2.03	0.36	1.01
H_2O	3.49	3.09	4.09	3.73	3.77	3.92
Total	100.12	100.65	100.83	100.34	100.14	99.63
Atoms per 12 [O. OH. F]						

Si	2.64	2.8	3.01	3.03	2.70	2.99
^{IV}Al	1.36	1.2	0.99	0.97	1.30	1.01
Sum Tet.	4.00	4.00	4.00	4.00	4.00	4.00
Ti	0.00	0.00	0.00	0.01	0.11	0.00
^{VI}Al	0.50	0.43	1.26	1.04	0.43	1.22
Fe	1.53	0.45	0.40	0.26	1.57	0.52
Mn	0.08	0.08	0.01	0.04	0.08	0.08
Mg	0.13	0.31	0.07	0.25	0.25	0.01
Ca	0.00	0.00	0.00	0.00	0.00	0.00
Li	0.62	1.20	0.77	0.65	0.65	0.66
Sum Oct.	2.86	2.47	2.51	2.25	3.09	2.49
K	0.91	0.87	0.90	0.80	0.86	0.78
Rb	0.03	0.03	0.01	0.02	0.01	0.02
Na	0.01	0.01	0.02	0.01	0.01	0.02
Sum A	0.95	0.91	0.93	0.83	0.88	0.82
F	0.26	0.69	0.19	0.41	0.09	0.22
OH	1.74	1.31	1.81	1.59	1.81	1.78

.000

This is a preprint, the final version is subject to change, of the American Mineralogist (MSA)
Cite as Authors (Year) Title. American Mineralogist, in press.
DOI: http://dx.doi.org/10.2138/am-2018-6196

.001

.002 **Table 2. LA-ICPMS analyses of trace elements in micas from three generations in veins, granite and greisen. Zr, U, Y, and REE were also analyzed**

.003 **but were systematically below 1 ppm.**

LA-ICPMS	Spot	Mg (ppm)	±	Ti (ppm)	±	Mn (ppm)	±	Co (ppm)	±	Nb (ppm)	±	Mo (ppm)	±	Sn (ppm)	±	Ba (ppm)	±	Ta (ppm)	±	W (ppm)	±
	1	7500	52	781.3	8.1	4835	28	3.04	0.11	0.622	0.027	0.033	0.041	436.6	3.3	121.8	1.5	0.0061	0.0043	28.75	0.43
	2	12003	82	853.2	7.9	5390	32	3.82	0.11	0.476	0.021	0.085	0.039	335.1	2.8	149.7	1.6	0.0094	0.0042	19.53	0.59
	3	16040	100	1039	11	6554	80	2.94	0.11	1.217	0.04	0.109	0.049	281.9	2	153.4	2.1	0.0379	0.0065	5.02	0.17
	4	16800	120	936.1	8.7	8199	46	2.528	0.088	1.319	0.041	0.132	0.043	226.8	2.1	136.5	1.4	0.0363	0.0066	6.72	0.21
	5	17880	110	966.7	8.6	8033	46	2.9	0.092	1.372	0.036	0.107	0.046	319.4	2.7	135.9	1.5	0.0453	0.0076	6.46	0.19
	6	16170	110	690.6	7.8	5741	49	1.879	0.085	0.796	0.027	0.111	0.043	339.2	2.7	131.6	1.3	0.0256	0.0051	4.94	0.19
	7	10104	98	609.1	5.3	2191	16	1.199	0.065	0.489	0.023	0.046	0.038	748.1	5.9	107.3	1.4	0.0149	0.0044	2.56	0.13
	8	11531	86	450.2	5.6	2398	15	0.878	0.058	0.237	0.016	0.026	0.035	738.2	6.1	133.7	1.7	0.0062	0.0036	2.71	0.14
Fe-Li-mca$_{1-I}$	9	15816	91	593.4	5.5	5085	27	2.248	0.078	0.681	0.027	0.082	0.039	423	9	140.9	1.8	0.0205	0.0046	4.19	0.15
	10	13241	82	448.7	5.7	3012	28	1.142	0.064	0.348	0.02	0.029	0.035	409.4	4.3	137	1.7	0.0048	0.0036	3.48	0.14
	11	12963	77	329.6	4.8	1612	13	0.839	0.055	0.313	0.021	0.02	0.045	470.2	3.1	127.8	1.7	0.0146	0.0057	1.71	0.1
	12	8628	49	272.7	4.3	1622.9	9.8	0.937	0.064	0.245	0.018	0	0.036	610.3	4.2	125.4	1.5	0.0161	0.0057	1.95	0.11
	13	16169	98	199.4	3.4	830.9	5.9	0.623	0.047	0.099	0.011	0.011	0.038	217	1.6	187	2.2	0.0074	0.0042	1.125	0.083
	14	17290	130	209.7	3.7	933	8.5	0.633	0.047	0.106	0.011	0.055	0.043	243.3	2.2	185.5	2.3	0.0086	0.004	1.18	0.082
	15	13490	84	614.4	9.6	3102	23	1.017	0.06	0.618	0.028	0	0.037	705.5	5.7	130.7	1.5	0.0217	0.0051	2.86	0.14
	16	10470	100	509.8	5.6	3396	20	1.272	0.066	0.573	0.026	0.033	0.037	435.6	3	133.1	1.7	0.03	0.0059	3.47	0.13
	17	10697	94	248.9	4.1	1761	14	0.844	0.05	0.212	0.016	0.013	0.03	295.9	2.2	144.1	1.7	0.0146	0.005	1.708	0.09

									1				5		8					1
	18	16150	140	225.6	4.3	1369	17	0.663	0.046	0.165	0.013	0.058	0.036	274.2	3.5	164.1	2	0.0068	0.0039	1.439	0.088
	19	15870	140	188.3	3.3	754.3	7.3	0.625	0.04	0.113	0.012	0	0.029	230.2	2.5	177.2	2.1	0.0118	0.0042	1.018	0.068
	20	17480	200	199.6	3.4	719	10	0.597	0.044	0.101	0.011	0.1	0.044	319	3.2	162	2	0.015	0.0042	1.079	0.068
	1	11283	58	367.7	4.1	1059.2	6.3	3.93	0.12	0.28	0.015	0.013	0.025	388.5	2.8	76	1.1	0.008	0.0033	21.49	0.34
	2	10467	61	454.5	4.4	1000.9	6.4	3.68	0.094	0.317	0.016	0	0.019	389.6	3.7	80.4	1.1	0.01	0.003	21.87	0.37
	3	12117	86	352.7	5.5	1075.3	8.7	4.438	0.098	0.347	0.017	0.01	0.023	376.9	4.1	77.5	1.2	0.011	0.003	21.58	0.35
	4	13124	86	342.3	4.1	916.7	8.7	4.06	0.12	0.316	0.018	0.013	0.026	425.2	4.5	73.4	1.1	0.0123	0.0034	20.95	0.34
	5	11990	100	417.2	4.3	1077.9	8.8	4.1	0.12	0.351	0.019	0.039	0.027	392.3	4.9	80.4	1.4	0.0071	0.0031	20.82	0.41
	6	9731	72	406.9	5.1	1252.6	9.9	3.621	0.095	0.258	0.016	0.013	0.024	411.6	4.6	80.4	1.2	0.0036	0.0025	21.23	0.35
	7	10308	86	392.8	5	1051.6	9.6	3.76	0.11	0.276	0.017	0.012	0.024	384.2	4.3	85.7	1.3	0.0077	0.0029	22.68	0.41
	8	8050	69	413.3	4.7	1322	11	3.71	0.098	0.2	0.012	0	0.019	389	4.9	79.2	1.2	0.0016	0.002	21.34	0.36
Fe-Li-mca$_{2\text{-}I}$	9	8506	79	346.3	4.6	1405	11	3.57	0.12	0.22	0.017	0	0.023	399.5	5.1	80.6	1.4	0.0015	0.0025	22.66	0.4
	10	5877	36	464.4	4.6	2538	18	2.549	0.083	0.468	0.024	0.069	0.033	422.3	4.5	110.1	1.4	0.0045	0.0031	31.28	0.45
	11	9310	48	524	5.8	1342.5	8.1	3.73	0.1	0.275	0.019	0.031	0.031	373	2.7	88.9	1.3	0.0081	0.0042	22.38	0.35
	12	9874	72	361.7	4.3	891	11	3.562	0.098	0.511	0.024	0	0.025	385.6	2.4	87	1.1	0.0175	0.0039	25	0.39
	13	11140	59	363.9	4	1037	12	3.82	0.099	0.714	0.025	0.023	0.028	388	2.9	98.1	1.2	0.0187	0.0037	25.82	0.35
	14	8043	53	411.6	5.4	1301.7	6.9	3.466	0.085	0.202	0.013	0.018	0.024	384.4	2.6	81.5	1	0.0057	0.0025	23.28	0.32
	15	12620	180	428.8	4.5	972.2	9	3.863	0.089	0.493	0.02	0.018	0.024	435	5.2	91	1	0.0162	0.0031	22.57	0.36
	16	10185	75	531.5	4.3	1528	14	3.746	0.097	0.262	0.015	0.018	0.028	387.8	3.2	88.8	1.1	0.0128	0.0033	21.09	0.33
	17	9480	130	426.4	4.1	1091.3	9.9	3.782	0.09	0.276	0.013	0.016	0.021	394.8	2.9	87.79	0.94	0.0098	0.0029	24.56	0.36
	18	9048	56	513.4	5.5	1276.1	6.6	3.498	0.09	0.316	0.015	0	0.02	398.6	2.	95.2	1	0.0094	0.003	22.45	0.33

									4				2		8				1		
Fe-Li-mca$_{4}$-III	1	21990	110	193	3.5	534.5	2.9	0.589	0.052	0.057	0.011	0.013	0.043	459.5	3.9	151	1.9	0.0019	0.0038	1.025	0.08
	2	19844	82	204.4	3.4	593.4	2.8	0.68	0.049	0.067	0.011	0.021	0.043	493.2	3.5	160.5	1.6	0.0034	0.004	1.101	0.089
	3	20853	90	200.8	3.4	554.4	2.9	0.659	0.052	0.0628	0.0098	0.151	0.068	478.5	3.9	152.2	1.6	0.002	0.0039	1.016	0.091
	4	21350	140	190.3	3.2	673.8	4.5	0.792	0.053	0.11	0.011	0.002	0.037	429.6	6.1	169.7	1.8	0.0096	0.0046	1.26	0.096
	5	18460	100	195.5	3.2	696.2	4.2	0.617	0.043	0.121	0.013	0.026	0.039	415.5	3.4	179	1.8	0.0028	0.0041	1.269	0.091
	6	18220	110	202.1	3.3	719.6	4.5	0.698	0.05	0.144	0.013	0.29	0.099	414.2	5.3	164.6	1.8	0.015	0.0049	1.96	0.25
	7	21200	130	186.9	3.2	398.8	4.4	0.716	0.049	0.0461	0.0082	0.24	0.26	820.2	5.9	128	1.4	0.0082	0.004	1.45	0.16
	8	39430	660	229.6	3.8	1640	65	1.824	0.089	0.0343	0.0075	0.014	0.039	1063	11	97.8	1.2	0.0057	0.0034	0.885	0.095
	9	20290	130	192	3.3	542.3	3.6	0.646	0.046	0.0639	0.0091	0	0.035	532.4	3.7	149.6	1.7	0.0072	0.0039	1.003	0.078
	10	15390	130	217.2	3.4	816	5.5	0.787	0.053	0.191	0.015	0.026	0.042	534.6	4.2	148.9	1.7	0.0233	0.0053	1.76	0.11
	11	27270	190	188.3	3	1230.9	9.1	2.083	0.085	0.119	0.011	0.098	0.048	440	4	160.7	1.8	0.0162	0.0043	1.377	0.093
	12	69690	640	187	3.3	3826	35	10.83	0.23	0.091	0.011	0.074	0.047	742.9	7.1	103.3	1.4	0.0117	0.0038	2.8	0.62
	13	18980	190	183.6	2.9	704.2	6.6	0.808	0.055	0.126	0.011	0.05	0.037	305.7	2.8	175.7	2	0.0176	0.0042	1.091	0.081
	14	19860	150	188.9	3.2	538	4.3	0.645	0.045	0.055	0.0093	0.008	0.034	566.9	4.6	144.6	2	0.0079	0.0035	1.373	0.084
	15	67500	500	180.1	3.3	3826	30	10.91	0.21	0.097	0.011	0.084	0.053	619.5	5.3	102.8	1.6	0.0132	0.004	1.21	0.11
	16	20820	330	191.1	3.2	740	15	0.992	0.069	0.104	0.01	0.019	0.033	321.9	7.4	168.3	1.8	0.0227	0.0041	1.202	0.081
	17	20510	170	195.5	3.1	651.4	5.8	0.712	0.043	0.0591	0.0088	0.047	0.039	367	3.5	158.3	1.6	0	0.0037	1.149	0.071
	18	20080	150	195.2	2.7	517.8	3.9	0.713	0.051	0.0229	0.0069	0	0.028	596.4	5.4	133	1.5	0	0.0034	1.009	0.075
	19	20600	160	203.8	3.1	600.7	4.8	0.689	0.045	0.1039	0.0072	0.027	0.03	444.7	4.5	145.8	1.5	0.0664	0.0042	1.093	0.075
	20	17900	180	198.9	3.3	764.9	9.3	0.793	0.046	0.293	0.012	0.001	0.032	364	3.1	167.3	1.8	0.2328	0.0055	1.127	0.07

Granite	1	13250	410	3400	770	3730	840	4.4	1	154	37	0.79	0.26	98	21	36.9	2.6	36.8	8.8	11	2.4
	2	12850	450	6300	1100	6200	1000	7.2	1.3	263	46	1.22	0.36	165	26	103	14	39.5	7.3	37.7	7.3
	3	11100	170	9200	150	9730	130	11.67	0.6	441.8	7	1.34	0.35	229	4.2	26.4	1.6	159.3	3	5.4	0.5
	4	11950	250	9100	160	9730	160	11.08	0.4	435.1	5.8	1.88	0.35	243.1	3.7	122.3	3.4	129.7	2.7	5.07	0.44
	5	12030	240	8910	150	9650	140	11.01	0.48	425.3	6.7	1.9	0.36	246	3.1	1006	27	126.6	2.4	5.27	0.37
	6	11310	250	8490	160	9410	120	10.74	0.56	415.3	6.1	1.3	0.25	241.9	4.7	643	13	120.6	3	6.23	0.48
	7	12130	250	8230	130	10020	140	11.78	0.54	447.9	7.6	1.46	0.4	249	4.5	69.1	2.6	158.8	3.3	6.33	0.37
	8	11320	190	9450	180	9870	120	10.98	0.49	442.2	8.1	1.6	0.38	243.1	4.4	15.77	0.99	119.2	2.6	5.23	0.34
	9	11050	160	8190	120	9330	120	10.68	0.43	410.8	6.7	0.9	0.26	238.4	4.2	215.9	4.3	225.8	3.9	6.15	0.39
	10	11410	220	8040	140	9700	130	10.88	0.47	420.5	7.3	0.76	0.28	239.6	3.7	129.2	3	235.1	4	6.94	0.5
	11	11460	260	9420	110	10000	100	10.88	0.49	459.6	5.6	1.34	0.3	239.5	3.9	11.88	0.86	163.5	3.2	6.21	0.45
	12	10850	150	9230	150	9800	140	11.76	0.57	442.4	6.7	1.12	0.34	231.3	4.6	6.75	0.7	152.7	3.9	5.18	0.41
	13	11510	220	9470	180	9650	140	11	0.43	460.1	7.5	1.1	0.3	236.7	4	79.9	4.1	155	3.9	4	0.33
	14	11810	240	9930	140	10030	120	11.74	0.61	428.6	6.1	1.36	0.28	244.7	4	34.1	1.5	91.6	1.7	4.47	0.41
	15	12350	310	10910	150	10070	100	11.75	0.55	412.7	5.2	1.76	0.37	252.2	3.8	100.6	3.1	39.35	0.76	2.28	0.22
	16	12230	300	10980	160	9670	110	11.17	0.54	384.2	5.2	2.06	0.4	250.4	4.1	1134	22	59.1	1.4	4.33	0.32
	17	11680	200	9250	130	10100	120	11.63	0.58	442.7	5.9	1.19	0.31	241.8	3.7	139.8	7.1	156.3	3	4.8	0.36
	18	11310	120	8920	110	10000	100	11.1	0.64	431	5.2	0.93	0.29	240.3	3.9	33.9	1.6	178.1	2.3	7.77	0.44
	19	11400	170	9070	120	9500	120	11.04	0.44	432.6	6.4	1.28	0.27	236.7	3.1	110	2.7	185.8	3.2	6.46	0.44
	20	11130	240	8120	160	9080	120	10.4	0.55	382.4	6.6	0.59	0.24	236.4	4.5	200.9	7.9	191.2	3.8	7.77	0.48
Greisen	1	366.9	7.4	394	16	10420	150	2.03	0.33	39.53	0.88	0.08	0.33	516.8	8.3	54	2.1	10.24	0.39	26.7	1.1

2	464	9.4	624	22	11900	140	2.28	0.28	55	1.2	0.29	0.35	566.3	8.1	55.3	1.9	15.13	0.39	30.2	1.1
3	573	10	1205	28	11480	130	2.34	0.34	69.2	1.4	0	0.3	535.8	7.4	55.7	1.9	17.8	0.48	25.6	1.3
4	254.6	5.3	197.4	8.7	13180	140	1.7	0.28	44.97	0.98	0	0.27	595	11	45.3	1.9	8.85	0.28	33.9	1.2
5	410	13	476	29	10460	200	1.2	0.43	43	2	0.09	0.57	505	12	59.3	4.8	11.58	0.56	24.3	1.8
6	425	14	379	23	10230	190	0.93	0.36	34.7	1.4	0.19	0.42	516	11	53.8	2.9	9.21	0.5	22.6	1.6
7	927	13	517	22	7891	95	1.62	0.28	44.41	0.95	0	0.25	492.3	7.9	56.3	2.4	9.16	0.28	26.1	1.1
8	513	12	515	21	9610	150	2.11	0.38	43.84	0.89	0.24	0.43	518.4	9.9	56.7	2.9	11.95	0.42	25.5	1.5
9	423	10	460	19	8860	120	1.8	0.3	43.8	1	0.13	0.32	532	10	57	2.9	11.86	0.41	27.7	1.3
10	422.1	9.2	405	17	9660	120	2.03	0.34	39.4	0.81	0	0.37	517.7	6.8	57.6	3.1	9.9	0.3	24.1	1.2
11	466.7	9.7	374	17	8230	100	1.95	0.37	37.78	0.96	0	0.26	511.9	8.5	56.5	2.6	8.98	0.37	24.9	1.1
12	1430	23	225	15	5572	65	1.08	0.24	27.62	0.77	0	0.27	532.7	8.2	46	2.9	6.17	0.28	28.9	1.4
13	806	16	689	24	8390	100	2.1	0.32	63.8	1.2	0	0.29	530.6	8.3	52.9	2.7	17.42	0.42	27.3	1.1
14	393.9	7.8	247	13	9780	130	1.85	0.31	35.56	0.72	0	0.26	539.9	8.5	58.2	2.4	8.17	0.33	28	1.2
15	2364	35	998	27	7515	88	1.74	0.25	111.6	1.5	0.03	0.27	606	10	31.7	2.1	28.94	0.66	36.5	1.4
16	2949	32	840	24	5148	53	1.74	0.29	111.9	1.9	0.48	0.29	722.6	8.1	66.8	2.4	19.24	0.57	51	1.7
17	2801	43	958	30	6186	76	1.69	0.23	118.4	2.2	0.1	0.22	727	12	55.7	2.3	18.44	0.48	52.8	1.4
18	505.7	9.2	277	16	7290	110	1.58	0.27	35.75	0.97	0.31	0.32	532	10	60.4	2.5	8.82	0.37	27.1	1.3
19	517	11	313	15	9410	200	1.99	0.39	35.69	0.86	0.13	0.22	504	13	52.5	3.2	7.87	0.3	24	1.1
20	616	16	966	29	14590	270	2.46	0.33	47.2	1.4	0.16	0.25	461	13	50.4	3	13.47	0.54	20.4	1.1

.004

This is a preprint, the final version is subject to change, of the American Mineralogist (MSA)
Cite as Authors (Year) Title. American Mineralogist, in press.
DOI: http://dx.doi.org/10.2138/am-2018-6196

Table 3. Electron microprobe analyses of chlorites from the Piaotang mineralized veins sampled at the level -388 m. Values preceded by the symbol '<' indicate element concentrations below the limit of detection.

	Chlorite$_{1\text{-}II}$	**Chlorite$_{2\text{-}III}$**																			
EPMA (wt%)	representative data	**388-13-2**	**388-13-3**	**388-13-4**	**388-13-5**	**388-13-10**	**388-11-19**	**388-11-20**	**388-11-21**	**388-11-22**	**388-11-23**	**388-11-24**	**388-11-25**	**388-11-26**	**388-11-27**	**388-11-28**	**388-11-29**	**388-11-30**	**388-11-31**	**388-11-32**	**388-11-33**	**388-11-34**
Al2O3	18.16	20.97	20.27	21.04	21.47	21.23	20.04	19.79	20.04	20.74	20.61	20.88	19.62	20.9	21.45	17.48	20.82	20.54	19.9	21	20.38	21.04
SiO2	29.35	23.47	27.21	25.16	26.23	23.89	26.65	26.91	27.21	27.42	26.52	26.67	25.52	27.08	24.73	31.99	26.24	26.73	26.32	26.75	27.91	27.75
TiO2	<0.05	<0.05	<0.05	<0.05	<0.05	<0.05	<0.05	<0.05	<0.05	<0.05	<0.05	<0.05	<0.05	<0.05	<0.05	<0.05	<0.05	<0.05	<0.05	<0.05	<0.05	<0.05
Na2O	<0.07	<0.07	<0.07	<0.07	<0.07	<0.07	<0.07	<0.07	<0.07	<0.07	<0.07	<0.07	<0.07	<0.07	<0.07	<0.07	<0.07	<0.07	<0.07	<0.07	<0.07	<0.07
MgO	15.3	5.89	15.32	8.6	13.4	5.05	13.39	10.19	17.27	15.42	12.24	11.43	10.36	15.11	10.72	22.33	12.77	12.48	9	14.6	17.72	16.3
MnO	0.72	2.61	1.19	0.66	3.79	2.32	0.55	3.75	0.46	0.64	1.8	1.87	1.74	1.25	1.2	0.47	0.79	0.54	2.64	1.26	0.86	0.83
FeO	23.09	32.93	21.8	31.1	21.44	33.97	24.84	26.68	19.22	21.92	28.21	28.07	28.57	23.5	28.21	16.92	26.59	26.46	28.88	22.64	19.43	21.71
K2O	<0.07	<0.07	<0.07	<0.07	<0.07	<0.07	<0.07	<0.07	<0.07	<0.07	<0.07	<0.07	0.07	<0.07	<0.07	<0.07	<0.07	<0.07	0.18	<0.07	<0.07	<0.07
CaO	<0.07	0.11	<0.07	0.1	0.14	<0.07	<0.07	<0.07	0.1	<0.07	<0.07	<0.07	0.07	0.08	0.07	<0.07	<0.07	<0.07	<0.07	<0.07	<0.07	<0.07
Total	86.62	86.01	85.86	86.66	86.47	86.51	85.62	87.4	84.34	86.26	89.44	88.97	86.03	87.98	86.44	89.28	87.25	86.79	86.96	86.36	86.34	87.67
Atoms per 14 O																						
Si	3.08	2.68	2.88	2.77	2.79	2.71	2.87	2.91	2.88	2.87	2.79	2.82	2.82	2.82	2.70	3.14	2.80	2.86	2.88	2.83	2.89	2.86
Al^{IV}	2.24	1.32	1.12	1.23	1.21	1.29	1.13	1.09	1.12	1.12	1.21	1.18	1.18	1.18	1.30	0.86	1.20	1.14	1.123	1.17	1.11	1.14
Al^{VI}	0.92	1.51	1.40	1.51	1.48	1.55	1.41	1.43	1.38	1.44	1.35	1.42	1.37	1.38	1.46	1.15	1.41	1.44	1.45	1.44	1.37	1.41
Mg	1.32	1.00	2.41	1.41	2.12	0.85	2.15	1.64	2.73	2.41	1.92	1.80	1.71	2.34	1.75	3.26	2.03	1.99	1.47	2.30	2.73	2.50
Fe^{2+}	2.39	3.14	1.93	2.87	1.913	3.23	2.23	2.41	1.70	1.92	2.48	2.48	2.64	2.04	2.58	1.39	2.37	2.36	2.65	2.00	1.68	1.87
Mn	2.02	0.25	0.11	0.06	0.34	0.22	0.05	0.34	0.04	0.06	0.16	0.17	0.16	0.11	0.11	0.04	0.07	0.05	0.24	0.11	0.07	0.07
Ti	0.06	0.00	0.00	0.00	0.00	0.00	0.00	0.00	0.00	0.00	0.00	0.00	0.00	0.00	0.00	0.00	0.00	0.00	0.00	0.00	0.00	0.00

Na	0	0.00	0.00	0.00	0.00	0.00	0.01	0.00	0.00	0.00	0.00	0.00	0.01	0.00	0.01	0.00	0.01	0.00	0.01	0.01	0.00	0.01
K	0	0.00	0.00	0.00	0.00	0.00	0.00	0.00	0.00	0.00	0.00	0.00	0.01	0.00	0.00	0.00	0.00	0.00	0.02	0.00	0.00	0.00
Ca	0	0.01	0.00	0.01	0.02	0.00	0.01	0.01	0.01	0.01	0.01	0.00	0.01	0.01	0.01	0.00	0.00	0.00	0.00	0.00	0.00	0.00
Σcat Oct	5.74	5.64	5.74	5.79	5.51	5.64	5.79	5.48	5.81	5.77	5.76	5.71	5.72	5.77	5.79	5.81	5.82	5.80	5.57	5.74	5.79	5.79
R2+	4.42	4.14	4.34	4.28	4.03	4.08	4.38	4.05	4.43	4.33	4.41	4.28	4.34	4.39	4.32	4.65	4.40	4.35	4.12	4.30	4.41	4.37
R3+	2.29	3.00	2.60	2.78	2.93	2.99	2.59	2.75	2.54	2.61	2.67	2.72	2.68	2.65	2.85	2.05	2.67	2.62	2.74	2.70	2.54	2.60
Fe/(Fe+Mg)	0.46	0.76	0.44	0.67	0.47	0.79	0.51	0.60	0.38	0.44	0.56	0.58	0.61	0.46	0.60	0.30	0.54	0.54	0.64	0.46	0.38	0.43
K2O+Na2O+CaO	0.1	0.12	0.06	0.1	0.14	0.03	0.13	0.06	0.1	0.08	0.06	0.05	0.2	0.13	0.13	0.08	0.04	0.03	0.22	0.08	0.03	0.04

.007

This is a preprint, the final version is subject to change, of the American Mineralogist (MSA)
Cite as Authors (Year) Title. American Mineralogist, in press.
DOI: http://dx.doi.org/10.2138/am-2018-6196

1008 **Figure 1**

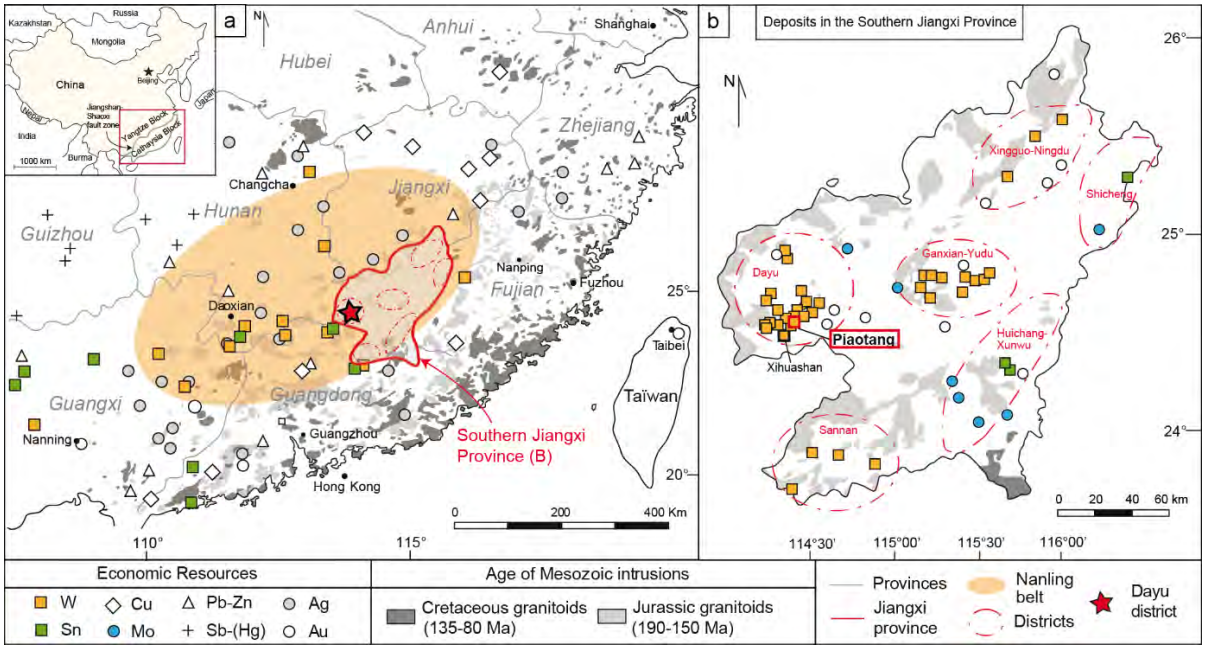

1009

1010 **Figure 2**

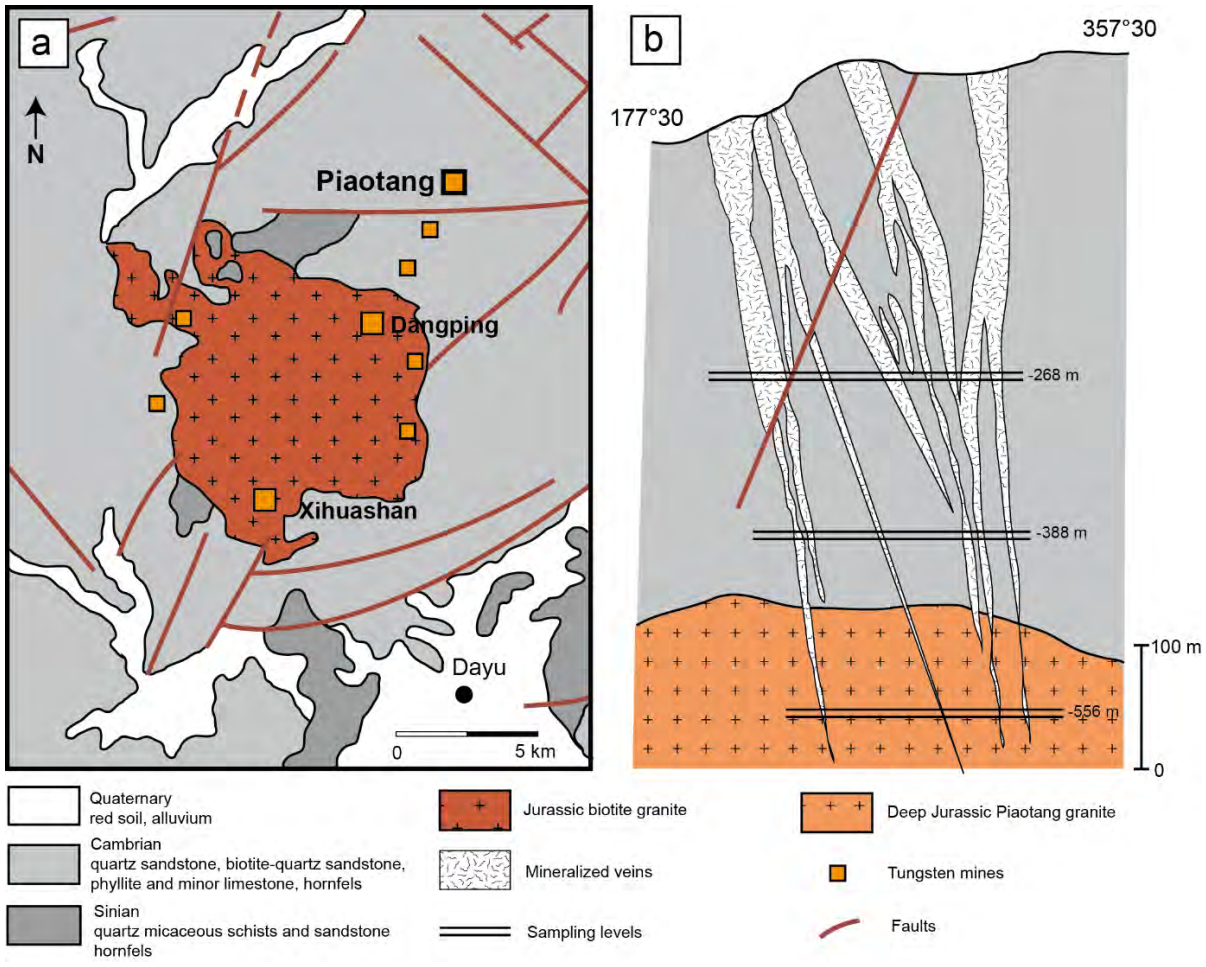

1011

This is a preprint, the final version is subject to change, of the American Mineralogist (MSA)
Cite as Authors (Year) Title. American Mineralogist, in press.
DOI: http://dx.doi.org/10.2138/am-2018-6196

1012 **Figure 3**

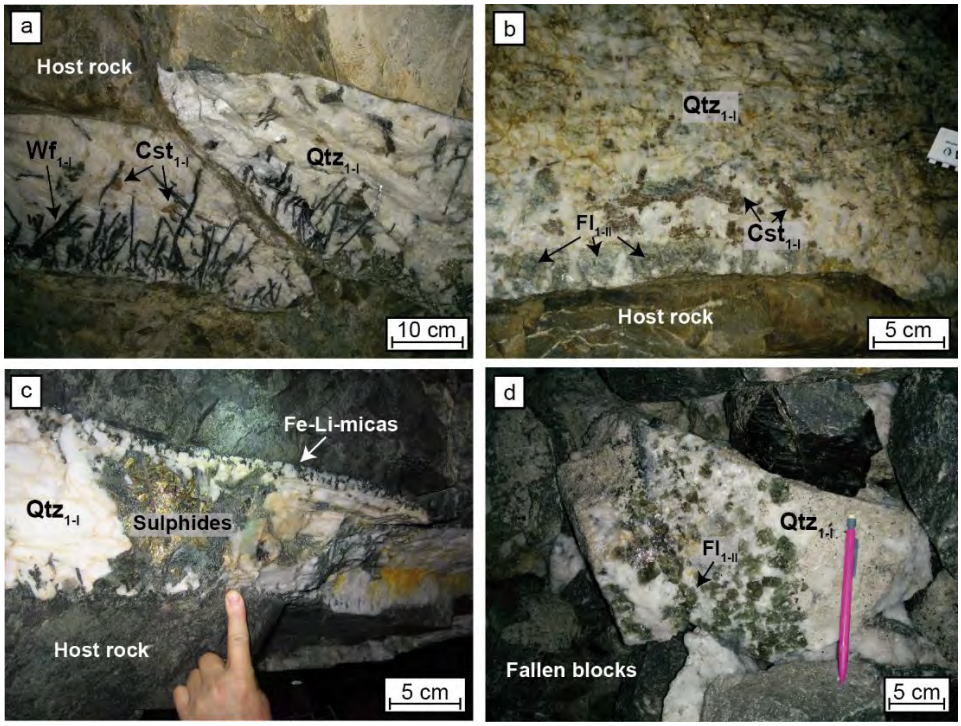

1013

1014 **Figure 4**

1015

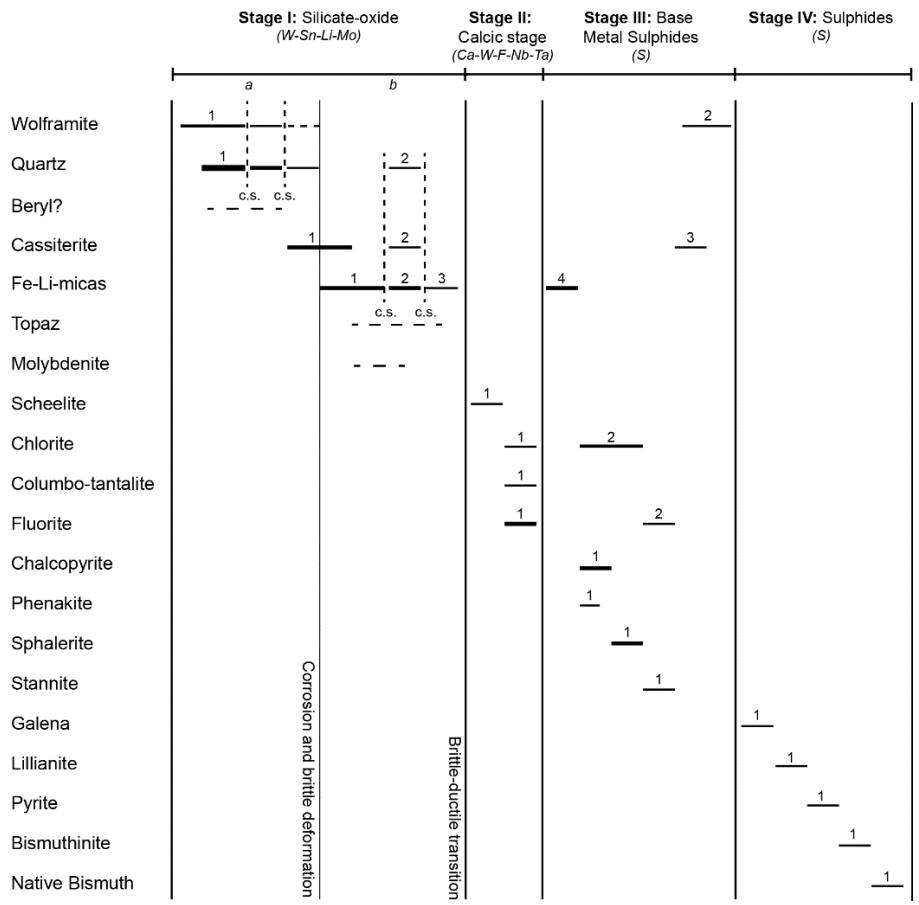

1016

This is a preprint, the final version is subject to change, of the American Mineralogist (MSA)
Cite as Authors (Year) Title. American Mineralogist, in press.
DOI: http://dx.doi.org/10.2138/am-2018-6196

1017

Figure 5

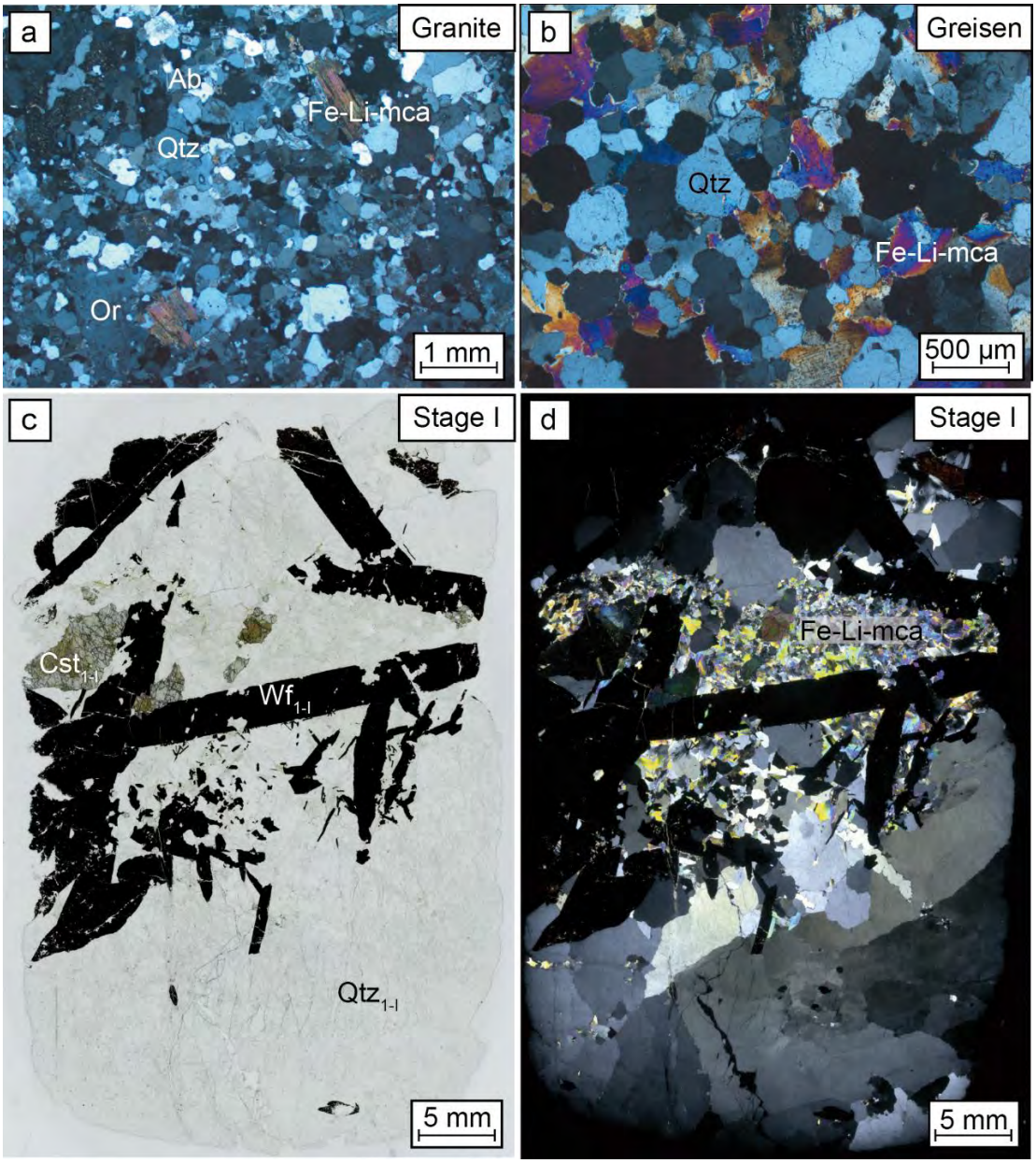

1018

1019

This is a preprint, the final version is subject to change, of the American Mineralogist (MSA)
Cite as Authors (Year) Title. American Mineralogist, in press.
DOI: http://dx.doi.org/10.2138/am-2018-6196

1020

Figure 6

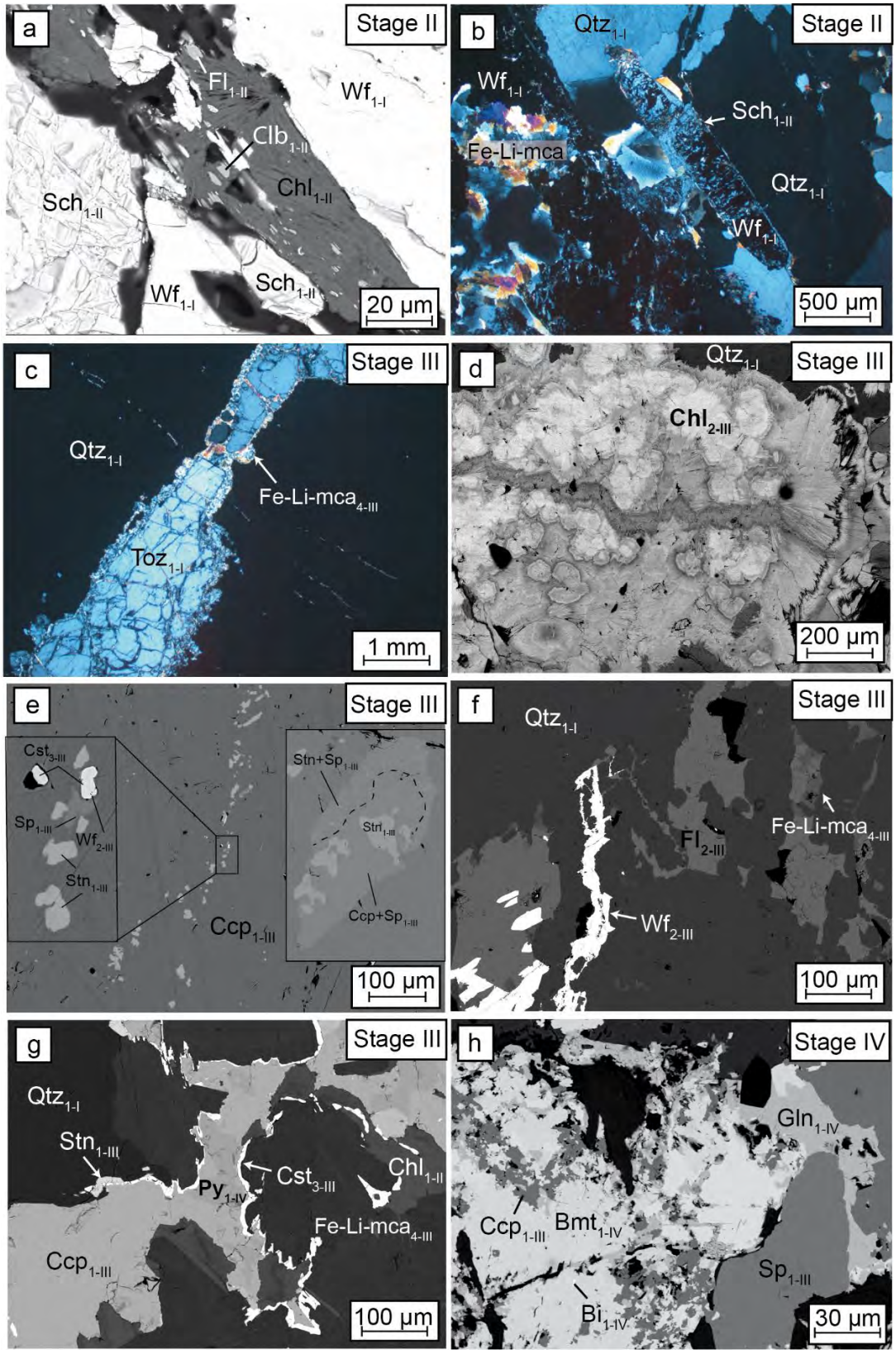

1021

1022

This is a preprint, the final version is subject to change, of the American Mineralogist (MSA)
Cite as Authors (Year) Title. American Mineralogist, in press.
DOI: http://dx.doi.org/10.2138/am-2018-6196

1023

Figure 7

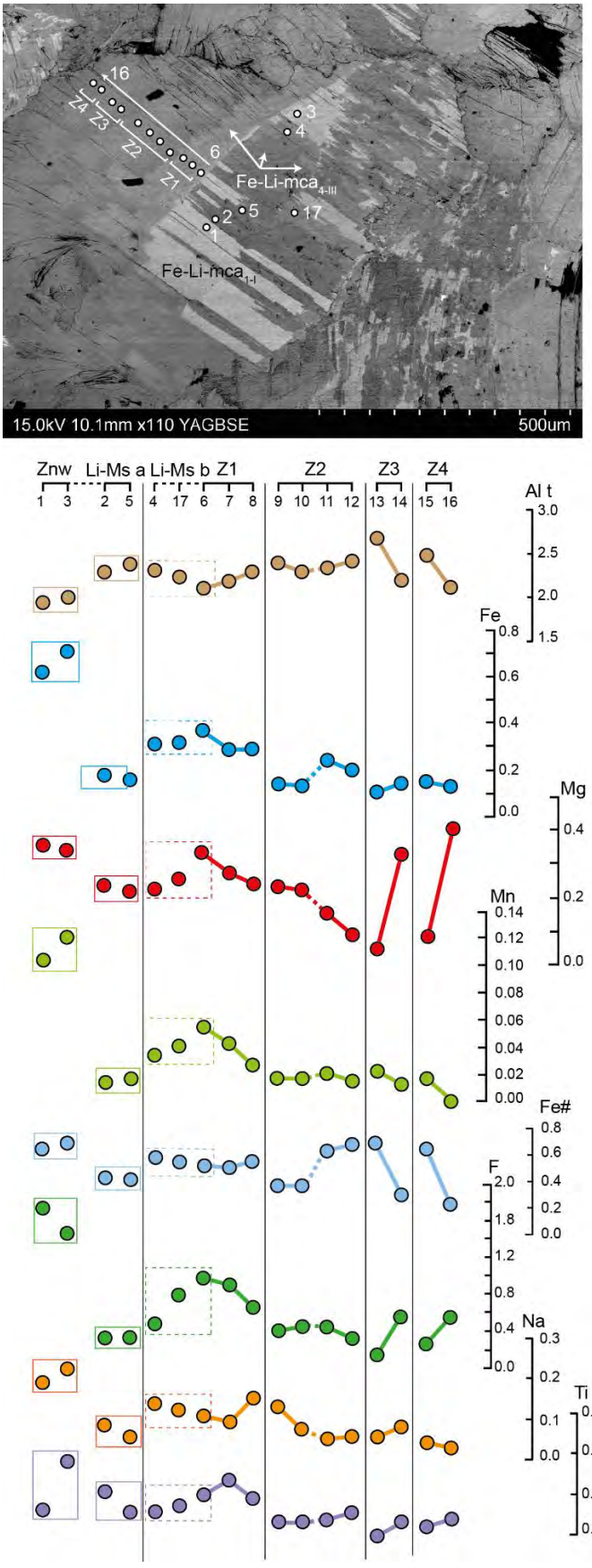

1024

This is a preprint, the final version is subject to change, of the American Mineralogist (MSA)
Cite as Authors (Year) Title. American Mineralogist, in press.
DOI: http://dx.doi.org/10.2138/am-2018-6196

1025 **Figure 8**

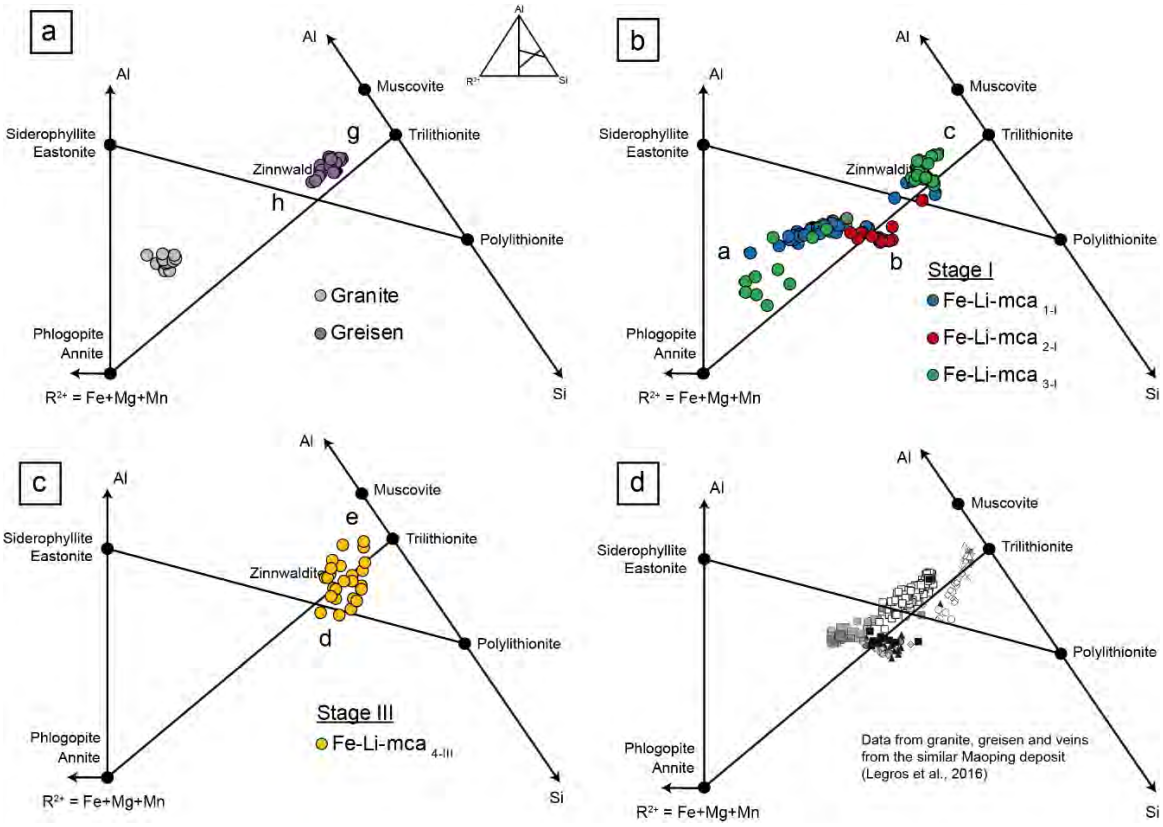

1026

1027

1028

1029

1030

1031

1032

1033

1034

1035

1036

1037

1038

This is a preprint, the final version is subject to change, of the American Mineralogist (MSA)
Cite as Authors (Year) Title. American Mineralogist, in press.
DOI: http://dx.doi.org/10.2138/am-2018-6196

1039

Figure 9

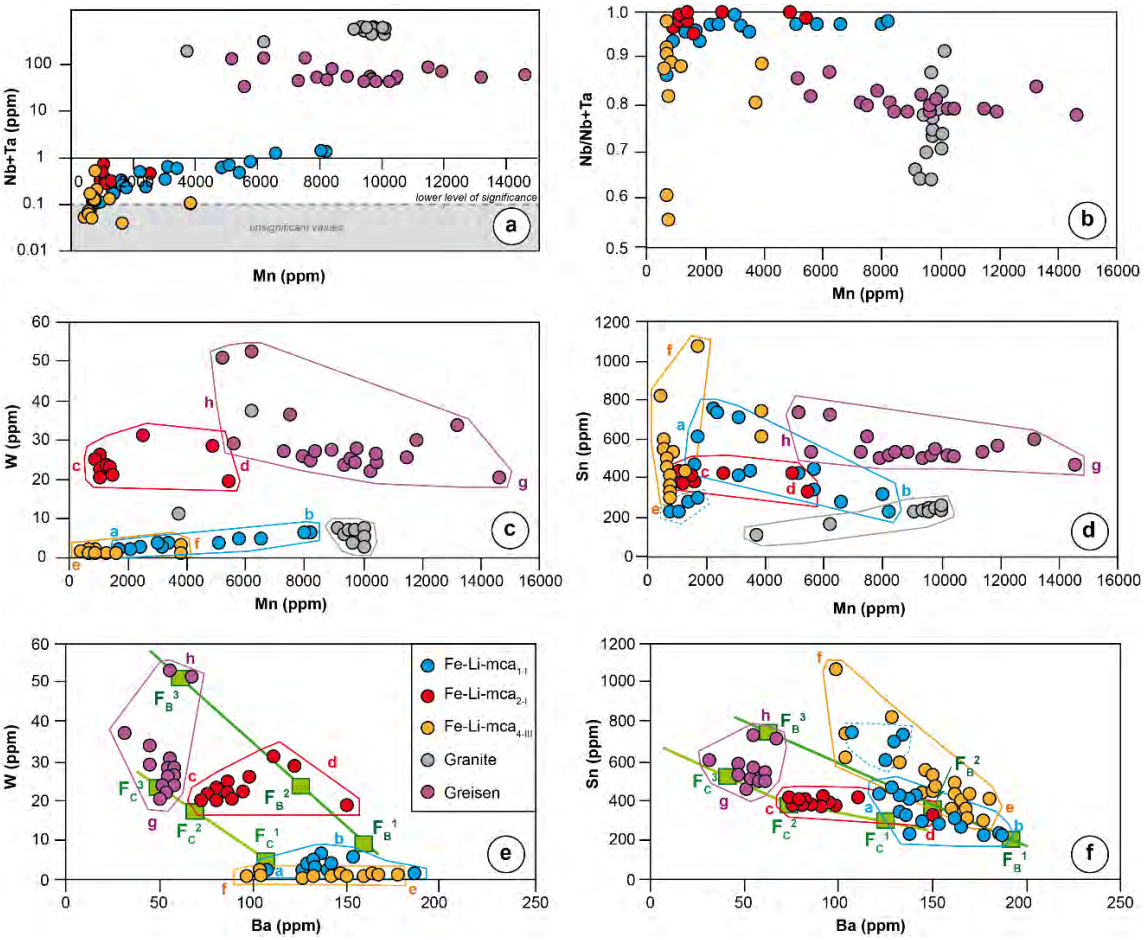

1040

1041

1042

1043

1044

1045

1046

1047

1048

1049

1050

1051

This is a preprint, the final version is subject to change, of the American Mineralogist (MSA)
Cite as Authors (Year) Title. American Mineralogist, in press.
DOI: http://dx.doi.org/10.2138/am-2018-6196

1052 **Figure 10**

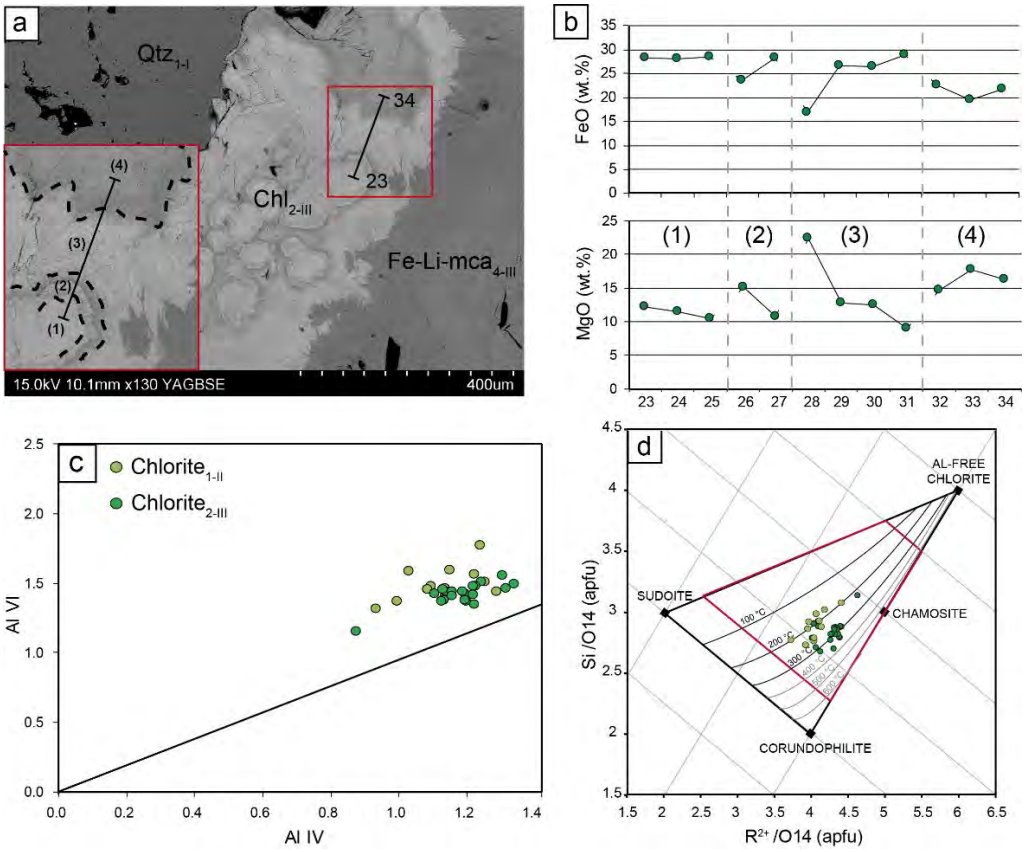

1053

1054 **Figure 11**

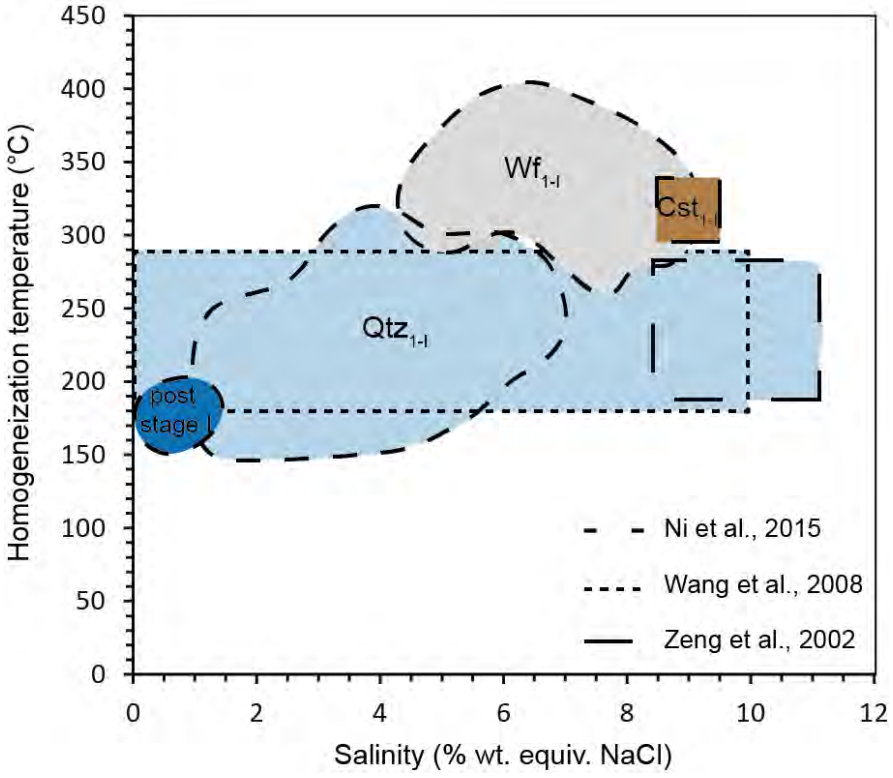

1055